

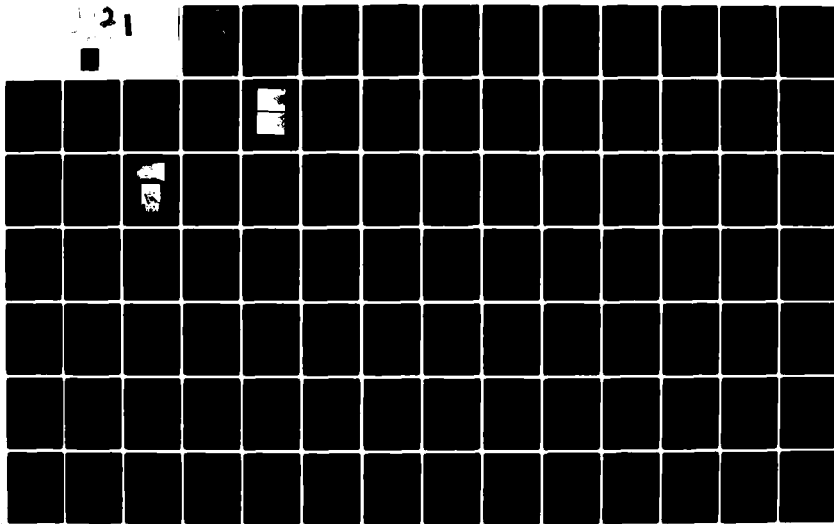
AD-A091 084

AIR FORCE INST OF TECH WRIGHT-PATTERSON AFB OH SCH00--ETC F/G 20/4
AN EXPERIMENTAL INVESTIGATION OF THE NEAR WAKE OF A CIRCULAR CY--ETC(U)
SEP 80 R E WALTERICK
AFIT/GAE/AA/805-1

UNCLASSIFIED

NL

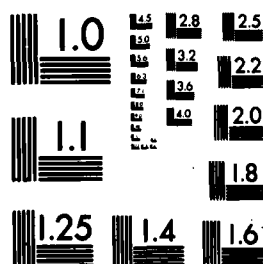
21



1 OF 2

AD

091084



MICROCOPY RESOLUTION TEST CHART
NATIONAL BUREAU OF STANDARDS-1963-A

LEVEL II

①

⑪ Sep 80

⑫ 102

DTIC
ELECTE
S NOV 04 1980 D
E

⑬ AN EXPERIMENTAL INVESTIGATION OF THE NEAR WAKE
OF A CIRCULAR CYLINDER

⑭ Master THESIS

⑮ AFIT/GAE/AA/80S-1 ⑯ RONALD CIV WALTERICK USAF

Eugene

Approved for public release; distribution unlimited

012225 Hm

AFIT/GAE/AA/80S-1

AN EXPERIMENTAL INVESTIGATION OF THE NEAR WAKE
OF A CIRCULAR CYLINDER

THESIS

Presented to the Faculty of the School of Engineering
of the Air Force Institute of Technology

Air University

in Partial Fulfillment of the
Requirements for the Degree of

Master of Science

by

Ronald E. Walterick, B.S.

Civ

USAF

Graduate Aerospace Engineering

September 1980

Accession For	
NTIS GRA&I	<input checked="checked" type="checkbox"/>
DDC TAB	<input type="checkbox"/>
Unannounced	<input type="checkbox"/>
Justification	
By _____	
Distribution/	
Availability Codes	
Dist.	Avail and/or special
A	

Approved for public release; distribution unlimited

ACKNOWLEDGEMENTS

An experimental investigation is, by nature, an effort involving many people of differing knowledge and skills. Although the entire effort coalesces under the direction of one principle investigator, he can by no means expect to complete each aspect of the project himself.

For their continued advice and support throughout my thesis quarters, I would like to thank my principle advisor, Dr. Harold Wright and the other thesis committee members, Dr. William Elrod and Dr. James Hitchcock. Whenever questions arose they gave graciously of themselves.

The experimental setup and operation would not have been possible without the unstinting efforts of Mr. William Baker, Mr. Harold Cannon, Mr. Nick Yardich, Mr. Scotty Whitt and Mr. Ken Arnold. To them my sincere thanks for their time and abilities.

The apparatus needed to conduct this investigation with were very professionally fabricated by Mr. Carl Shortt, Mr. Russell Murray and Mr. Ron Ruley of the Air Force Institute of Technology school shops. Their ingenuity and foresight are greatly appreciated.

For help in data gathering and analysis, I express my appreciation to Mrs. Ruth Sikorsky. Her efforts during this phase of the investigation were most welcome.

For her excellent typing efforts on behalf of my thesis, a special thanks to Mrs. Rachel Avant.

To my friend, Dr. George Catalano, I can never express my gratitude sufficiently for long and fruitful discussions, spent in an effort to elevate my technical competence. I hope that someday I can justify all of his efforts.

For fostering the desire to pursue a career in engineering, I shall forever be indebted to my parents. Through their efforts it has become possible.

Finally, to my wife Candice and daughter Jennifer, whose strength in the face of adversity has been an inspiration and guide for all of my efforts.

Ronald E. Walterick

CONTENTS

<u>Section</u>	<u>Page</u>
Acknowledgement	ii
List of Figures	vi
List of Tables.	viii
Symbols	ix
Abstract.	xii
I. Introduction	1
Background	1
Objectives	4
Approach	4
II. Experimental Apparatus and Procedure	6
Flow System.	6
Circular Cylinder	8
Laser Velocimeter System	10
III. Results and Discussion	17
Mean Velocities.	18
Turbulent Intensities.	36
Integral Time Scales	53
Taylor Time Microscales.	58
Kinetic Energy Dissipation Rates	58
IV. Conclusions.	63
V. Recommendations.	65
Bibliography.	66
Appendix A: Mean Velocity and Turbulent Intensity Data Reduction	68
Appendix B: Skewed Autocorrelation Function Correction Procedure	71

<u>Section</u>	<u>Page</u>
Appendix C: Ambiguity Noise Correction	75
Appendix D: Integral Time Scale Determination.	78
Appendix E: Taylor Time Microscale Determination	80
Appendix F: Particle Lag Estimation.	83
Vita	86

List of Figures

<u>Figure</u>		<u>Page</u>
1	Two Dimensional Circular Cylinder Near Wake Flowfield.	2
2	Pictorial View of Circular Cylinder Near Wake.	3
3	Laboratory Flow Facility	7
4	Cylinder Surface Pressure Coefficients	9
5	Circular Cylinder.	11
6	Laser Velocimeter Set-up	14
7	Pictorial View of Laser Velocimeter Set-up	15
8	Electronic Data Processing Scheme	16
9	Lateral Mean Velocity Profile, $X/2Ro=0.0$	19
10	Lateral Mean Velocity Profile, $X/2Ro=0.25$	20
11	Lateral Mean Velocity Profile, $X/2Ro=0.50$	21
12	Lateral Mean Velocity Profile, $X/2Ro=0.75$	22
13	Lateral Mean Velocity Profile, $X/2Ro=1.00$	23
14	Lateral Mean Velocity Profile, $X/2Ro=2.00$	24
15	Lateral Mean Velocity Profile, $X/2Ro=3.00$	25
16	Lateral Mean Velocity Profile, $X/2Ro=5.00$	26
17	Wake Half Width Growth	28
18	Development of Centerline Mean Velocities	30
19	Effect of Cylinder Rotation on Mean Velocities, $X/2Ro=0.0$, $Y/2Ro=0.34$; $X/2Ro=0.75$, $Y/2Ro=0.6$	31
20	Effect of Cylinder Rotation on Lateral Mean Velocities, $X/2Ro=-0.50$	33
21	Effect of Doppler Shift on Mean Velocities	37
22	Lateral Turbulent Intensity Profile, $X/2Ro=0.0$	39
23	Lateral Turbulent Intensity Profile, $X/2Ro=0.25$	40

<u>Figure</u>	<u>Page</u>
24 Lateral Turbulent Intensity Profile, $X/2Ro=0.50$	41
25 Lateral Turbulent Intensity Profile, $X/2Ro=0.75$	42
26 Lateral Turbulent Intensity Profile, $X/2Ro=1.00$	43
27 Lateral Turbulent Intensity Profile, $X/2Ro=2.00$	44
28 Lateral Turbulent Intensity Profile, $X/2Ro=3.00$	45
29 Lateral Turbulent Intensity Profile, $X/2Ro=5.00$	46
30 Development of Centerline Turbulent Intensities	49
31 Effect of Cylinder Rotation on Turbulent Intensities, $X/2Ro=0.0$, $Y/2Ro=0.34$; $X/2Ro=0.75$, $Y/2Ro=0.6$	50
32 Effect of Cylinder Rotation on Lateral Turbulent Intensities, $X/2Ro=-0.50$	52
33 Effect of Doppler Shift on Turbulent Intensities	54
34 Development of Longitudinal Integral Time Scales	56
35 Development of Longitudinal Taylor Time Microscales	59
36 Development of Centerline Kinetic Energy Dissipation Rates	62
37 Autocorrelation Function With Skewness	72
38 Autocorrelation Function Corrected for Skewness	74
39 Autocorrelation Function for Integral Time Scale Determination	79
40 Autocorrelation Function for Taylor Time Microscale Determination	81

List of Tables

<u>Table</u>		<u>Page</u>
I	Digital Autocorrelation Function data, X/2Ro=-3.13, Y/2Ro=0.09	17
II	Effect of Marker Particle Concentration on Mean Velocities and Turbulent Intensities at X/2Ro=5.00, Y/2Ro=0.0.	34
III	Effect of Pinhole Diameter on Mean Velocities and Turbulent Intensities at X/2Ro=0.50, Y/2Ro=0.0; X/2Ro=-2.65, Y/2Ro=0.13 and X/2Ro=-2.13, Y/2Ro=0.09. . .	35
IV	Integral Time Scales	57
V	Taylor Time Microscales	60

Symbols

A	Radial distance from cylinder center
A_0, A_1, A_2	Coefficients of second order polynomial fit to autocorrelation function maxima
B_0, B_1, B_2	Coefficients of second order polynomial fit to autocorrelation function minima
C_0, C_1, C_2	Arithmetic mean of coefficients from parabolic fit to autocorrelation maxima and minima
C_D	Drag coefficient
C_P	Pressure coefficient
d	Separation distance of laser beams at focusing lens
d_T	Theoretical diameter of laser beam at focal point
d_*	Distance between $1/e^2$ points of laser beam
D	Marker particle diameter
D_0, D_2	Polynomial coefficients for a parabola
e	Base for natural logarithm
f	Focal length of lens
F_d	Doppler shift frequency of flow without phase modulator
F_d^*	Doppler shift frequency of flow with phase modulator
F	Frequency
F_0	Doppler frequency
\bar{K}	Stokes coefficient
l	Distance from focusing lens to control volume
L	Integral length scale
M	Mach number
N	Number of fringes in control volume
P	Pressure
P'	Power spectra function

\bar{Q}	Statistical property
r_o	Laser beam radius
R	Autocorrelation function
R_{e_p}	Reynolds number based on particle diameter
R_{e_D}	Reynolds number based on model diameter
R_o	Circular cylinder radius
R_1, R_2, R_3	Autocorrelation function maxima and minima
S	Fringe spacing
t	Time
T	Time of averaging
T_{IS}	Integral time scale
T_λ	Taylor time microscale
T_c	Time to first zero crossing of autocorrelation function
T_2	Time to autocorrelation second maximum
U	Mean velocity in longitudinal direction
U^*	Mean velocity with phase modulator
U_{FS}	Mean velocity of free stream
U_p	Mean velocity of particle
U_g	Mean velocity of gas
U_{IS}	Integral velocity scale
U_λ	Taylor velocity microscale
U'	Longitudinal component of fluctuating velocity
\underline{U}	Particle lag
V'	Lateral component of fluctuating velocity
X	Longitudinal distance from circular cylinder trailing edge
Y	Lateral distance from centerline of circular cylinder
Y_M	Wake half width

Z	Distance perpendicular to X Y plane
α	Half angle between laser beams at the control volume
β	Constant in particle lag calculations
ϵ	Kinetic energy dissipation rate
η	Refractive index
λ	Wavelength of laser beam
λ_T	Taylor length microscale
μ	Viscosity of fluid
θ	Location on cylinder surface
ρ	Density
ρ_p	Particle density
σ	Constant in ambiguity noise calculations
τ	Sample time
ω	Cylinder rotation rate
ΔF	Frequency shift
ΔF_0	Root mean square deviation from doppler frequency
ΔY	Change in lateral direction

(\quad) Time average

Subscripts

FS	Free stream
IS	Integral scale
MAX	Maximum
REF	Reference
RMS	Root mean square
λ	Taylor microscale

Abstract

The near field region of the turbulent wake behind a stationary ($\omega=0$ RPM) and rotating ($\omega=500$ RPM) two dimensional circular cylinder is documented. U component mean velocities, turbulent intensities and velocity autocorrelation functions are measured at various downstream locations. From the autocorrelation functions, Taylor time microscales, longitudinal integral time scales and energy dissipation rates are computed. The free stream velocity and Reynolds number, based on cylinder diameter, are respectively 5.9 m/sec and approximately 50,000. The turbulent measurements are made with a laser velocimeter using a frequency shifting phase modulator and the photon correlation processing scheme. Naturally occurring contaminant is augmented with vaporized kerosene to increase the magnitude of scattered light. Results are presented for the effects of varying angular speed, frequency shifting, particle concentrations and detector optics pinhole size on the turbulent quantities.

I INTRODUCTION

Background

Several studies have been completed at the Air Force Institute of Technology utilizing a Laser Doppler Velocimeter system in conjunction with the photon correlating scheme (References 1, 2, 3 and 4). A common factor of all of these studies has been the use of naturally occurring flow contaminant to obtain laser beam light scattering. The present study was conceived as a further demonstration of the LDV's capabilities, by studying the flow about a two dimensional circular cylinder with naturally occurring contaminant augmented with flow seeding. The facility chosen for this investigation already existed in the form of the Air Force Institute of Technology two dimensional smoke tunnel. This facility possesses velocity ranges within the capability of the LDV and is ideally suited for marker particle seeding because of its inherent smoke generating system.

The choice of a two dimensional circular cylinder, as the model for study, was made because of the diversity of flow regions that comprise its flowfield (Figures 1 and 2). The turbulent near wake of this investigation can be described as incompressible, unsteady and initial condition dependent.

Available theory for two dimensional wakes is restricted to the far field region, where self preservation (the only change in the flow is in the length and velocity scales used to describe it) and Reynolds number similarity exist. The far field wake does not begin for ten diameters downstream of the cylinder.

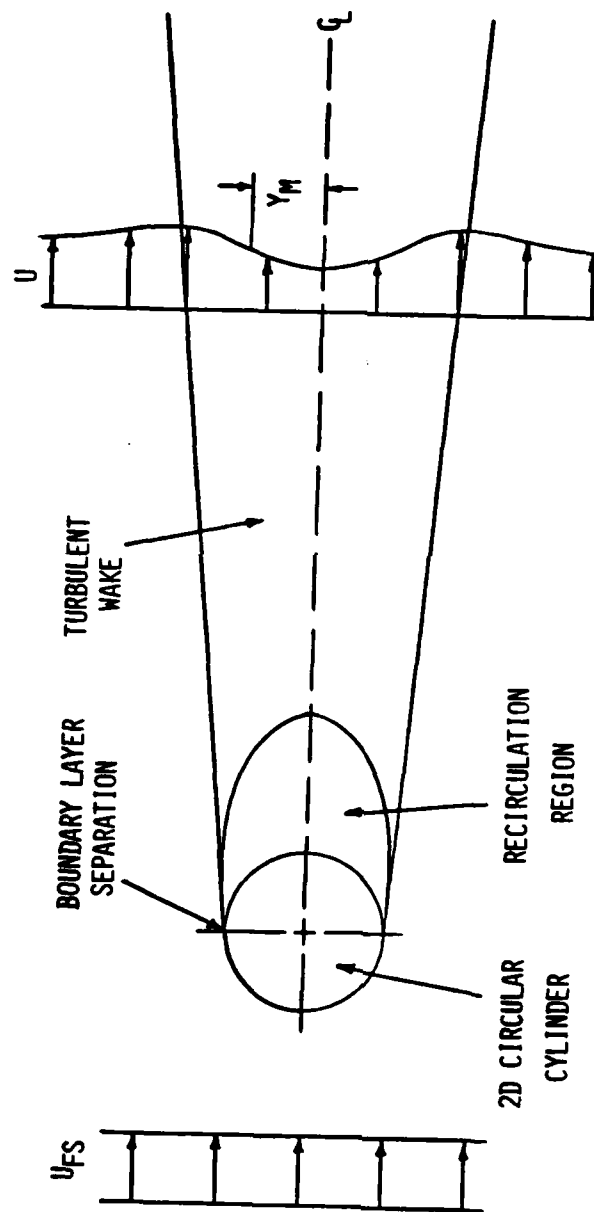


FIGURE 1. TWO DIMENSIONAL CIRCULAR CYLINDER NEAR WAKE FLOWFIELD

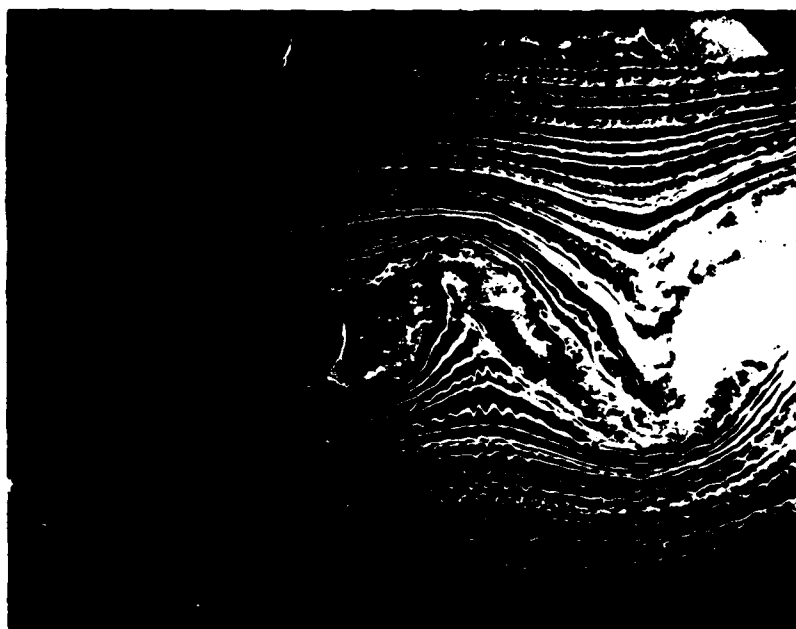


FIGURE 2. PICTORIAL VIEW OF CIRCULAR CYLINDER
NEAR WAKE

Experimental studies of the two dimensional wake of a circular cylinder are many, but their comparison to the present study is very restricted. Most work appears to have been centered about very low Reynolds number (<200) flows. The wake structure at these Reynolds' numbers (based on cylinder diameter) bears little resemblance to the present studies wake structure (Reynolds number based on cylinder diameter of 50,000).

The far field wake is treated to the practical exclusion of the treatment of the near wake. Measurements extend to only five cylinder diameters downstream in this investigation. The far wake theoretically does not commence until ten cylinder diameters downstream.

In many cases the cylinder does not span the entire width of the test section, resulting in three dimensional end effects. In essence few empirical results are available for exact comparison with the measurements taken.

Objective

The main objective of this investigation is to determine the validity of using the AFIT LDV system in an artificially seeded flow-field. The characterization of the two dimensional circular cylinder flowfield by measurements of mean velocity, turbulent intensity, integral time scales, Taylor time microscales and kinetic energy dissipation rates, is secondary in nature, but intimately tied into the main objective. Determination of the nature of the flowfield behavior is necessary for an accurate assessment of the effects of parametric studies.

Approach

The approach taken to meet the main objective of this study is to

conduct several parametric studies within the different flow regions behind the two dimensional circular cylinder. The study is conducted at one free stream velocity (5.9 meters/second). The parameters selected for variation are marker particle concentration, aperture size, frequency shift of the phase modulator and to a lesser extent rotation rate of the cylinder. The flowfield regions chosen for probing include the potential flow region above the cylinder, the boundary layer near the surface of the cylinder, the recirculating region behind the cylinder and the near wake, downstream of the recirculating region. An evaluation of the compatibility of the LDV in conjunction with the seeded flow system will be based on the effect of parametric variation on local mean velocity and turbulent intensity measurements and how they agree with expected results.

This investigation is herein documented with discussions of the experimental apparatus and procedure utilized, the results of the measurements, the conclusions drawn from these measurements, recommendations for follow-on investigations and appendices of detailed data reduction methods.

II EXPERIMENTAL APPARATUS AND PROCEDURE

Flow System

The facility used for this investigation is the Air Force Institute of Technology two dimensional smoke tunnel (Figure 3). This facility employs an open return system of flow, capable of subsonic incompressible velocities up to 23 meters/second, using two diffuser isolated 1.5 horsepower motor driven fans. Turbulent measurements are taken at a nominal freestream velocity of 5.9 m/sec and Reynolds number based on cylinder diameter (11.75 cm) of approximately 50,000. The velocity was monitored at first by a Prandtl type pitot probe and a micromanometer. These were later discarded in favor of the laser velocimeter, as a means of setting and checking the freestream velocity.

The removable front test section measures 1.5 m in length, 1.0 m in height and 0.07 m in width. The back wall of the test section is of laminated plate glass, whereas the front wall is of 0.0097 m thick plexiglass. This window arrangement is acceptable in light of the fact that the laser velocimeter is operated in the backscatter mode. The test section is noted as having a downhill gradient of 0.05 m in 1.5 m.

The flow marker particles are introduced into the flow system in thin streamtubes by a stack and injector apparatus, positioned in the tunnel contraction region. The stack is of airfoil shape with sixty five 0.60 cm inside diameter injector tubes issuing from it. The marker particles are generated in a process where, two 900 watt inconel heaters boil kerosene fuel at 605 degrees Kelvin, creating vapor particles that are then mixed under turbulent conditions with cool air to produce a dense white nontoxic and noncorrosive smoke. Water vapor is condensed out of the smoke in a condensing chamber prior

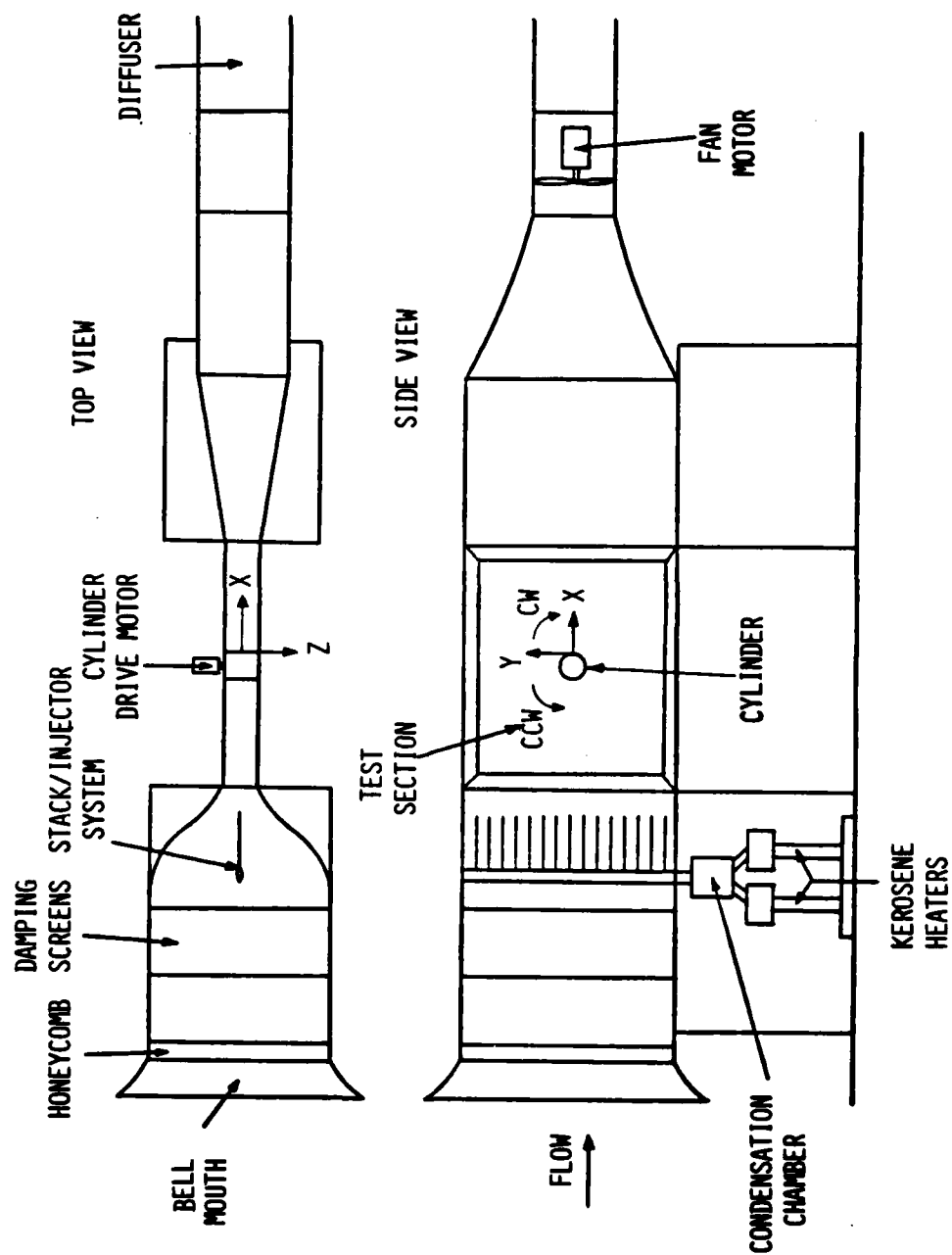


FIGURE 3. LABORATORY FLOW FACILITY

to entrance into the stack/injector apparatus, thereby eliminating water condensation in the injector tubes and the test section.

A great deal of prior effort was spent in reducing turbulence levels in this flow system (Reference 5). These efforts included installation of a 0.2 m radius bell mouth to the tunnel inlet, in an attempt to correct for a low contraction ratio of 11.5 to 1.0. Immediately downstream of this location a 0.076 m thick section of honeycomb, with a cell length to diameter ratio of 8.0, was installed to reduce large scale turbulent structures. In addition a series of screens (progressively finer downstream) were mounted prior to the stack/injector location. From measurements taken in the freestream, it would appear that turbulent intensities approach a value of 0.10 in the smoke streamtubes. Such high values must be attributed to the shape of the stack/injector system, its location and the process of issuing a secondary flow into the mainstream through the injectors (Reference 5).

Circular Cylinder

Two circular cylinders, one capable of rotation and one not, were constructed that mounted to the test section back wall in the approximate center (Figure 3). Both cylinders are of 0.059 m radius and 0.07 m thickness. This represents a test section area blockage ratio of 12%. One cylinder is constructed of polished wood with a static pressure orifice located at midspan. A positive seal with the test section sidewalls is achieved by capping each end of the cylinder with felt, thereby assuring two dimensional flow about the cylinder. A cylinder surface pressure survey was conducted (Figure 4) at two values of U_{FS} and is compared with inviscid theory and experimental measurements for subcritical flows (Reference 6).

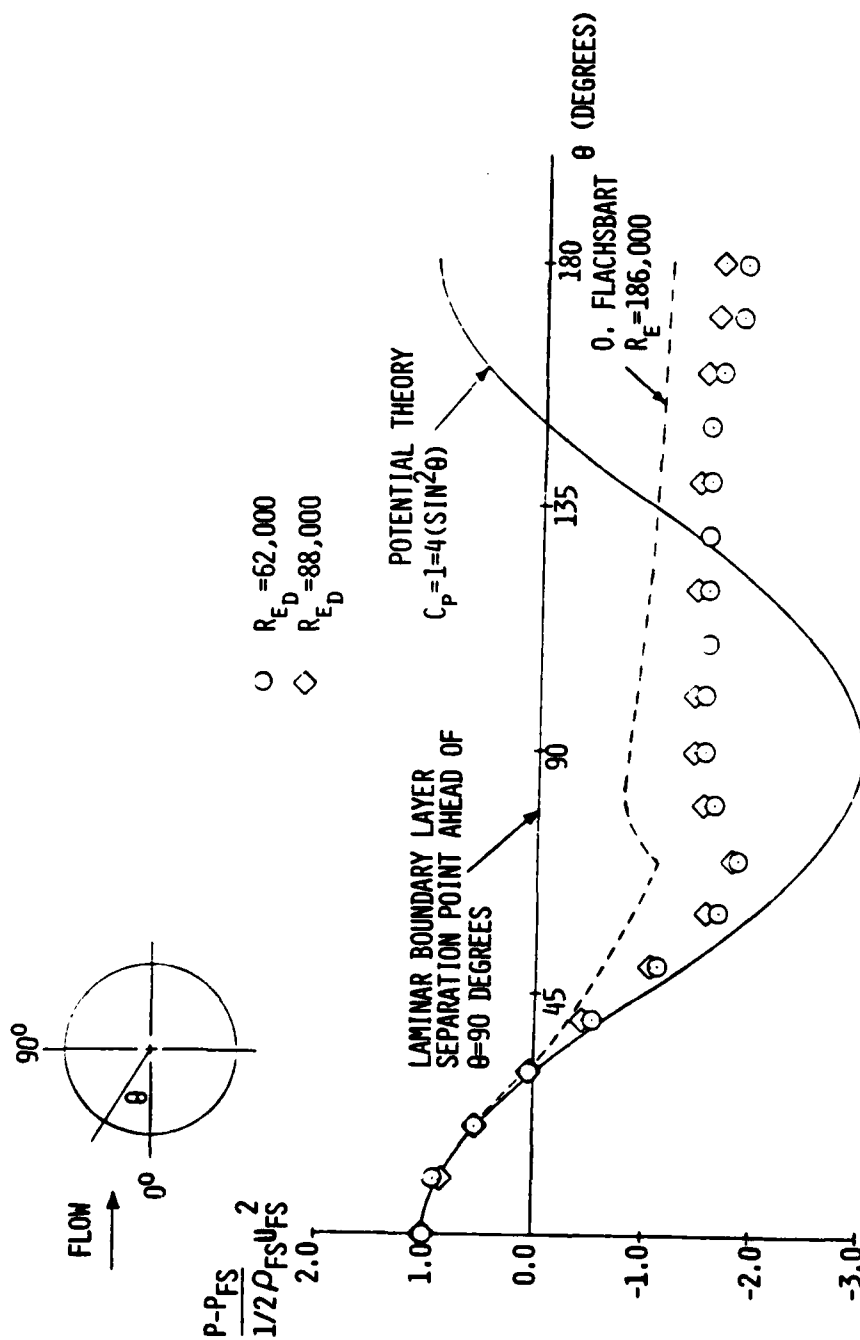


FIGURE 4. CYLINDER SURFACE PRESSURE COEFFICIENTS

The cylinder capable of rotation (Figure 5) is constructed of aluminum, with a smooth surface painted flat black to minimize scattering of light from its surface. Two endplates of plexiglass, one fixed and one free floating are mounted to either end. With the cylinder installed in the test section a gap of approximately 0.051 mm exists between the plexiglass endplates and aluminum main body. The possibility of three dimensional flow existing at the gap in the cylinder ends is considered negligible. Rotation of the cylinder is accomplished by mounting a small variable speed motor to a shaft extending from the cylinder main body through the back wall. Rotations of up to $\omega=800$ RPM are possible without any significant vibrations being introduced into the test system. Rotation rates are constant to within ± 5 RPM.

Laser Velocimeter

The laser used for all measurements is a Helium-Neon Laser of 15 milliwatts intensity at 6328.0×10^{-10} m, plus associated power unit. The laser beam diameter is 1.1 mm at the $1/e^2$ points. The transmitting optics consisted of a transmitter beamsplitter and polarization unit mounted to the laser head, a frequency shifting electro-optic phase modulating crystal, two front surface silvered plane mirrors mounted at 45 degrees to the horizontal and a convex focussing lens of 100 cm focal length. The beamsplitter takes the incident beam from the laser and divides it into two equal intensity, 1.1 mm diameter beams. The prisms used in this process are anti-reflection coated at 6328.0×10^{-10} m. Two adjustments to the laser beams are available. First, there is an adjustment for α (the half angle between the laser beams at the control volume). For this investigation the value of α is equal to a constant 0.6 degrees. Second, there is an adjustment for beam separation. A

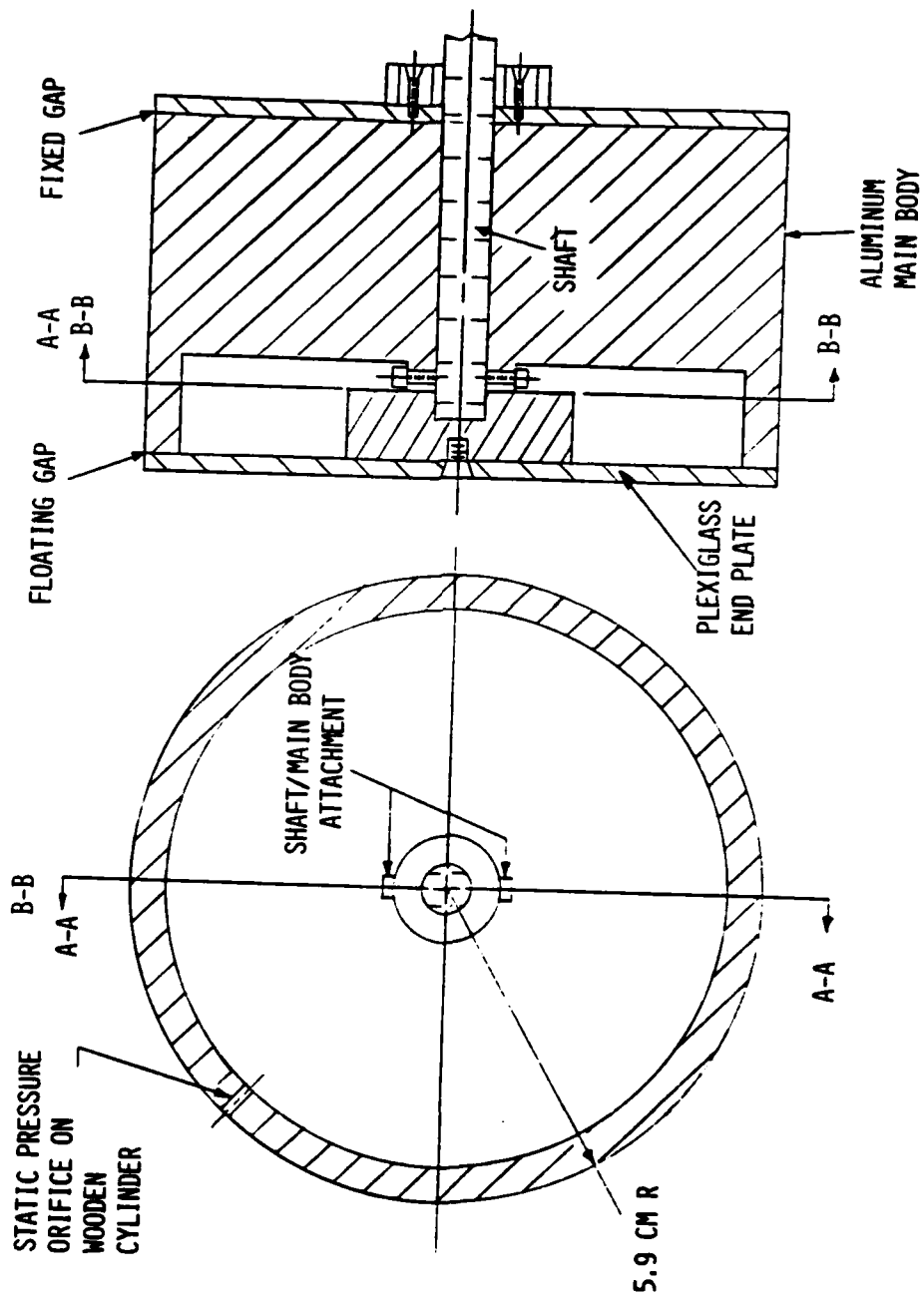


FIGURE 5. CIRCULAR CYLINDER

constant value of $l=20$ mm is maintained.

The frequency shifting phase modulator is required in the optical train to eliminate any flow direction sense ambiguities and provide measurements in regions of high turbulent intensity. In principle a uniform shifting of the fringes in the control volume (point of laser beam intersection) is possible with an application of a sawtooth voltage to the phase modulator's two electro-optical crystals. A resulting increase or decrease in the doppler frequency of the flow enables the flow direction to be determined. A drive unit is required for the phase modulator unit as well as a universal counter for accurate determination of the doppler frequency shift applied.

Two front surface silvered mirrors are required for transmission of the laser beams along the optical path. Both mirror surfaces are masked to eliminate stray light from being transmitted through the system. The convex focussing lens is made of high quality optical glass.

The receiving optics consists of a collecting lens/aperture and photo multiplier tube. The receiver photon detection unit employs a 200 mm telephoto lens as a spatial filter by being focused, with an external reflex viewer, onto the fringe control volume. The scattered light, from particles passing the alternate constructive and destructive interference fringes of the control volume, are focused onto a 400 μ m diameter pinhole prior to detection by the photo multiplier tube. The 400 μ m diameter pinhole provides the best signal to noise ratio for the current experimental setup. The associated photo multiplier tube power unit supplies a constant 1850 volts to the cathode of the photomultiplier tube.

The laser, transmitting optics and receiving optics are all mounted to a wood and metal optical bench (Figures 6 and 7). Flowfield longitudinal traverses are accomplished by translation of the entire bench. Lateral traverses are conducted with an aluminum secondary table capable of uniform translation through a chain and sprocket mechanism. The design of the secondary table limited lateral traverses in the -Y direction to $Y/2R_o = -1.0$. A traverse across the test section in the Z direction was conducted early in the investigation to determine the extent of two dimensional flow across the width. The resultant velocity profile indicated a uniform velocity 2.0 cm on either side of the test section centerline. All measurements were conducted at the centerplane of the test section.

The electronic processing scheme is composed of a digital photon correlator and data storage unit, associated power supply and oscilloscope for visual observation of the autocorrelation function growth with time. The correlator possesses a resolution time of from 50 nanoseconds to 1 second. Measurements were taken in the single clipped autocorrelation mode and at an infinite sample rate. A schematic of the electronic signal processing equipment is shown in Figure 8.

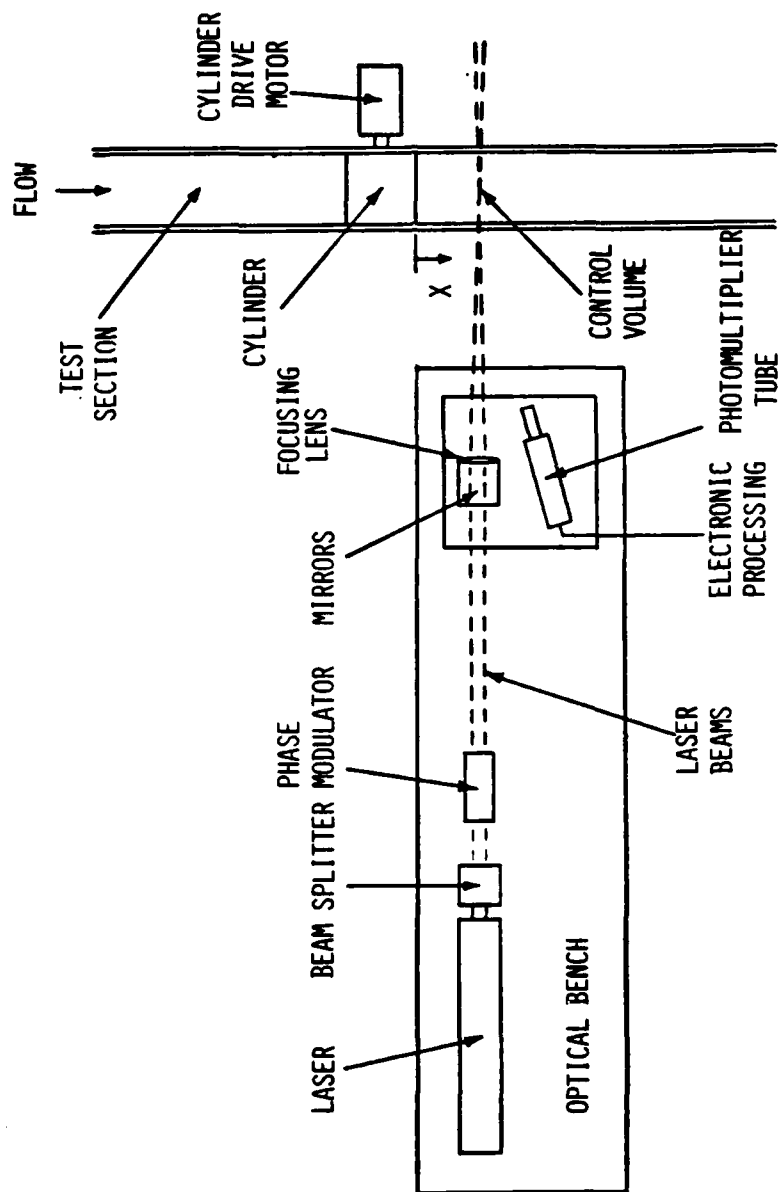


FIGURE 6. LASER VELOCIMETER SETUP

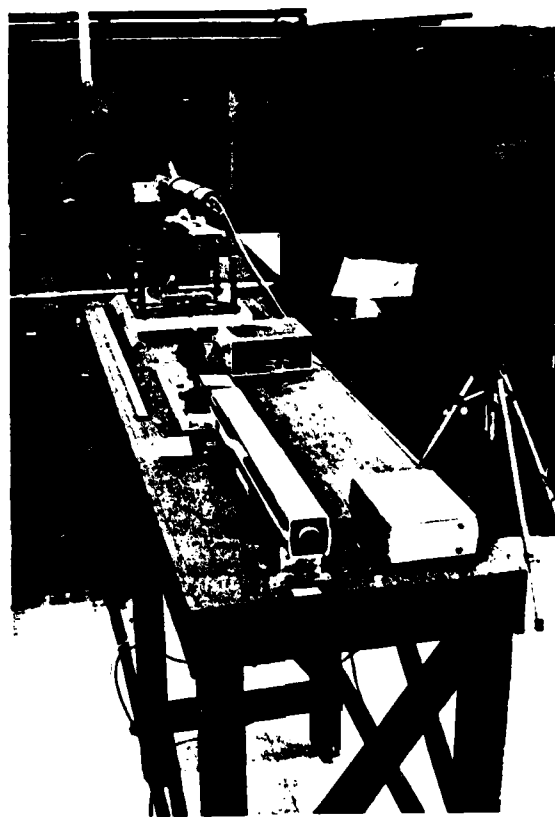
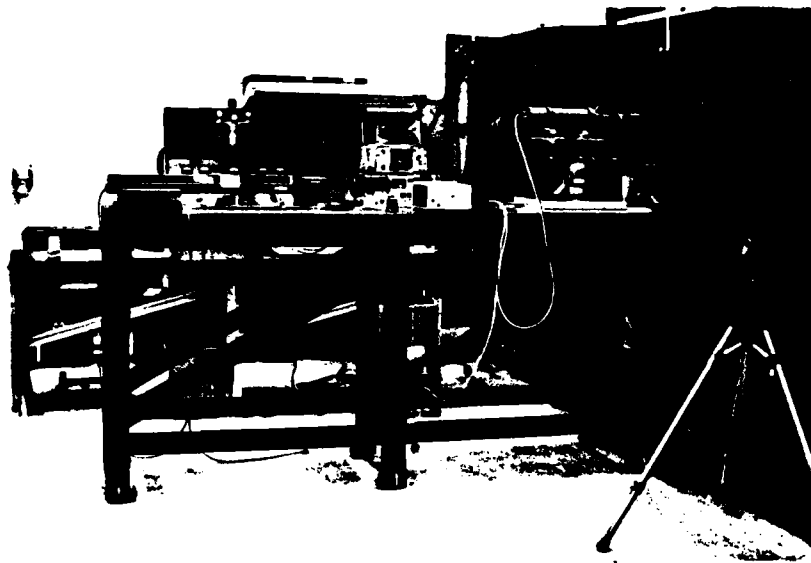


FIGURE 7. PICTORIAL VIEW OF LASER VELOCIMETER
SETUP

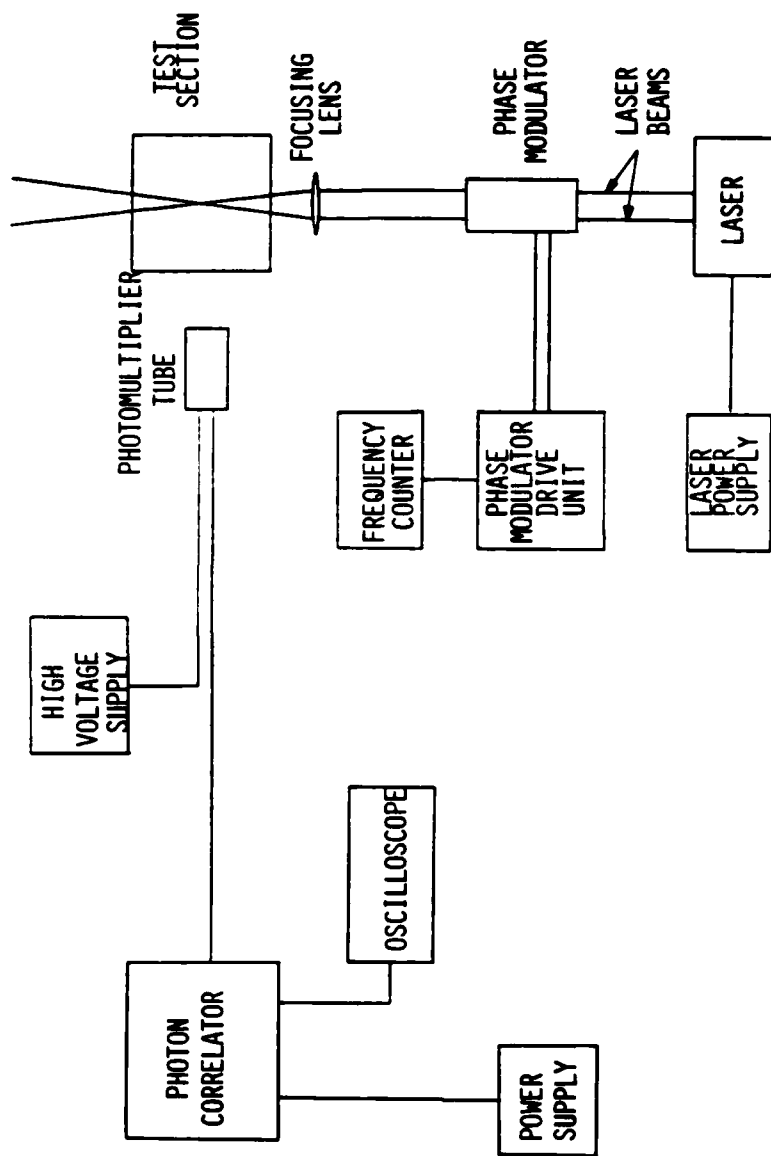


FIGURE 8. ELECTRONIC DATA PROCESSING SCHEME

III RESULTS AND DISCUSSION

Measurements are made in the near wake of a two dimensional circular cylinder of one point statistical properties. These properties consist of mean velocities, turbulent intensities and autocorrelation functions in the X direction. A sample of typical data is shown in Table I.

R(VOLTS, ARBITRARY)			T(μSECONDS)
2.08	1st	R _{MAXIMA}	0.0
2.06			.0031
2.02			.0063
1.96			.0094
1.90			.0125
1.84			.0156
1.80			.0188
1.77			.0219
1.76	1st	R _{MINIMA}	.0250
1.98	2nd	R _{MAXIMA}	.0531
1.72	2nd	R _{MINIMA}	.0781
1.88	3rd	R _{MAXIMA}	.1094
1.64	3rd	R _{MINIMA}	.1375
1.77	4th	R _{MAXIMA}	.1656
1.56	4th	R _{MINIMA}	.1969

TABLE I Digital Autocorrelation Function Data,
X/2Ro=-3.13, Y/2Ro=0.09

This data is a digital representation of a typical autocorrelation function (see Figure 37). It consists of hand recorded values of R(auto-correlation function ordinate in arbitrary volts) versus T(auto-correlation function abscissa in μseconds, i.e. delay time). From this data longitudinal mean velocities and turbulent intensities are computed as

detailed in Appendix A. If the autocorrelation function is skewed (as it was for this entire investigation) it must be corrected for skewness as shown in Appendix B. In addition to the skewness correction a correction for ambiguity noise must be applied to the autocorrelation function. This procedure is outlined in Appendix C. Integral time scales and Taylor time microscales are also computed from the skewness corrected autocorrelation function. These procedures are treated in Appendices D and E respectively. Finally, kinetic energy dissipation rates are estimated from the integral time scales and Taylor time microscales.

The effects of cylinder rotation, marker particle concentration, detector pinhole diameter and frequency shifting on the mean velocities and turbulent intensities are noted.

A laser doppler velocimeter is used to obtain all measurements.

Mean Velocities

Lateral mean velocity profiles are presented in Figures 9 to 16 for downstream locations $X/2R_o=0.0, 0.25, 0.50, 0.75, 1.00, 2.00, 3.00$ and 5.00 , with the cylinder both rotating and nonrotating. The profiles are assumed to be symmetrical about the wake centerline for the stationary case.

The local mean velocity is nondimensionalized by the free stream velocity and the lateral displacement is nondimensionalized by twice the cylinder radius.

Note the existence of a region of reverse flow behind the circular cylinder in Figures 9, 10 and 11. This recirculating region begins at $X/2R_o=0.0$ and decreases in width with increasing downstream location, until it terminates somewhere between $X/2R_o=0.75$ and $X/2R_o=1.00$

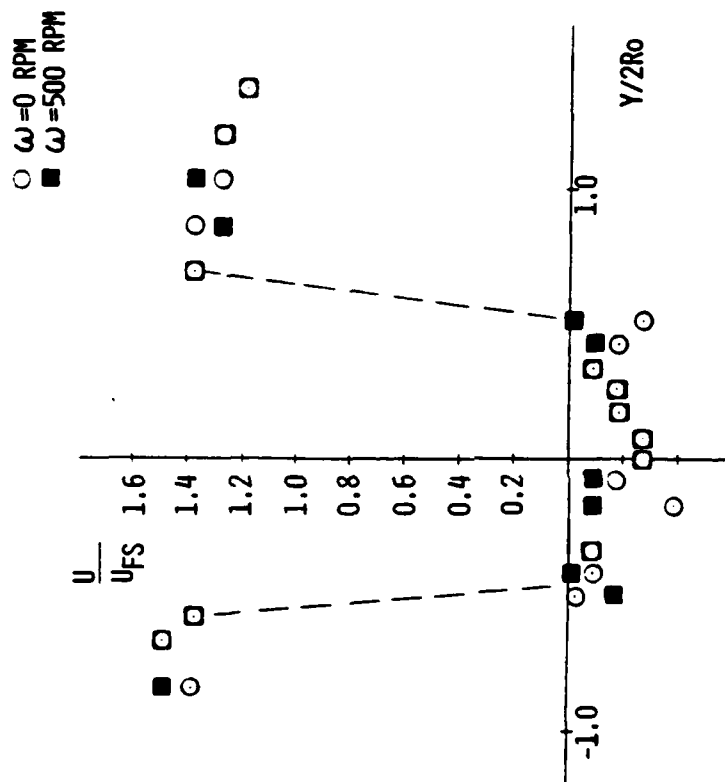


FIGURE 9. LATERAL MEAN VELOCITY PROFILE, $X/2R_o=0.0$

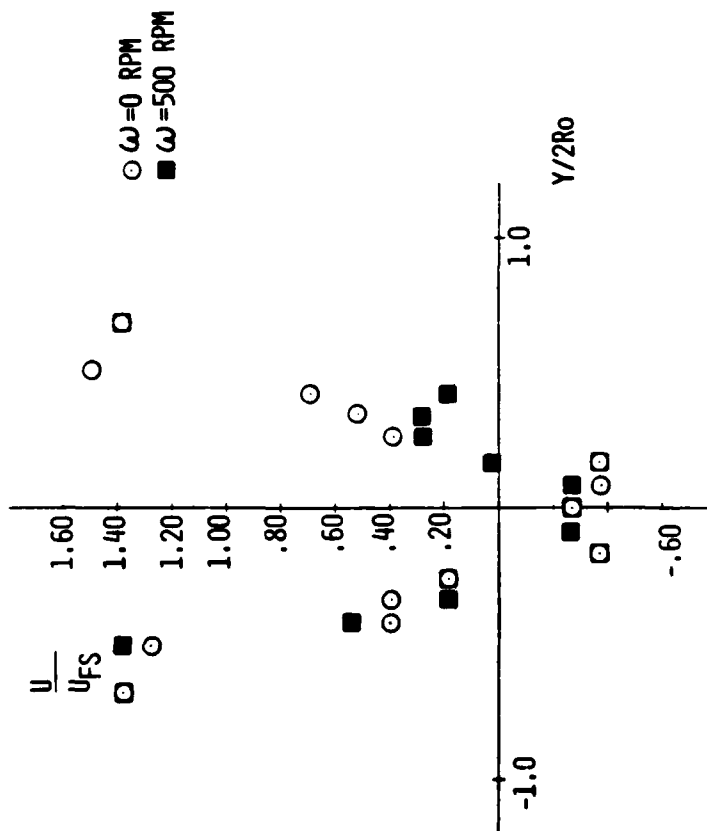


FIGURE 10. LATERAL MEAN VELOCITY PROFILE, $X/2R_o=0.25$

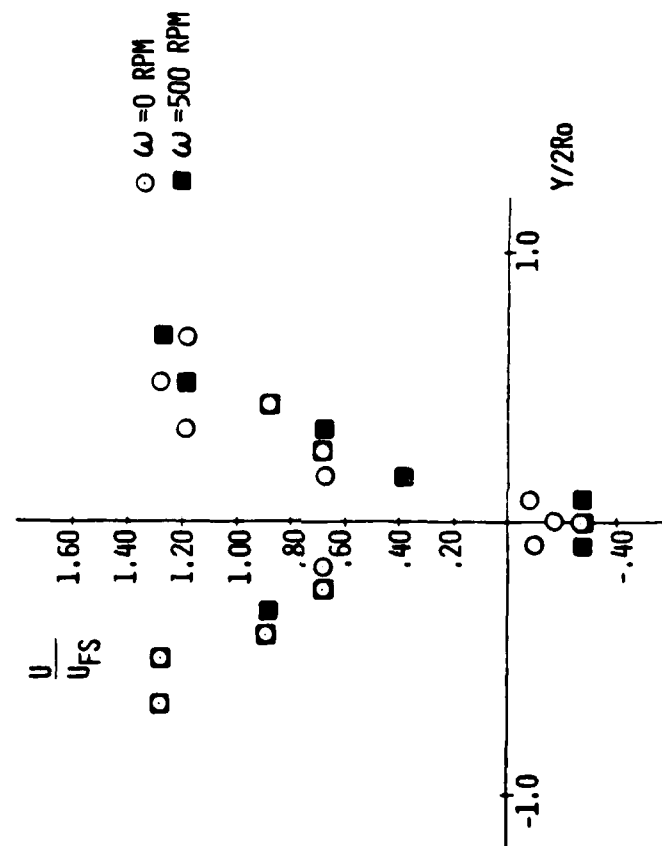


FIGURE 11. LATERAL MEAN VELOCITY PROFILE, $X/2R_0=0.5$

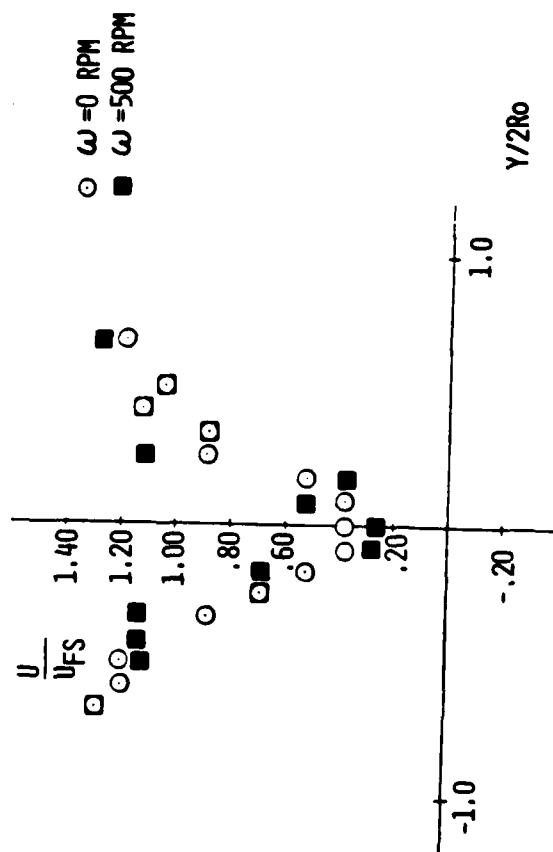


FIGURE 12. LATERAL MEAN VELOCITY PROFILE, $X/2R_o=0.75$

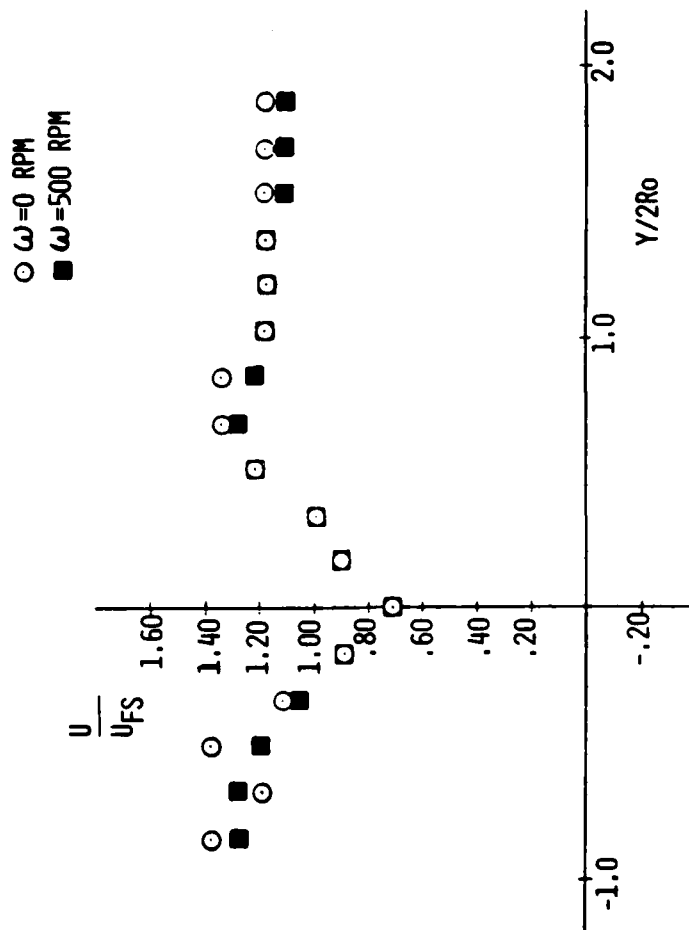


FIGURE 13. LATERAL MEAN VELOCITY PROFILE, $X/2R_o=1.0$

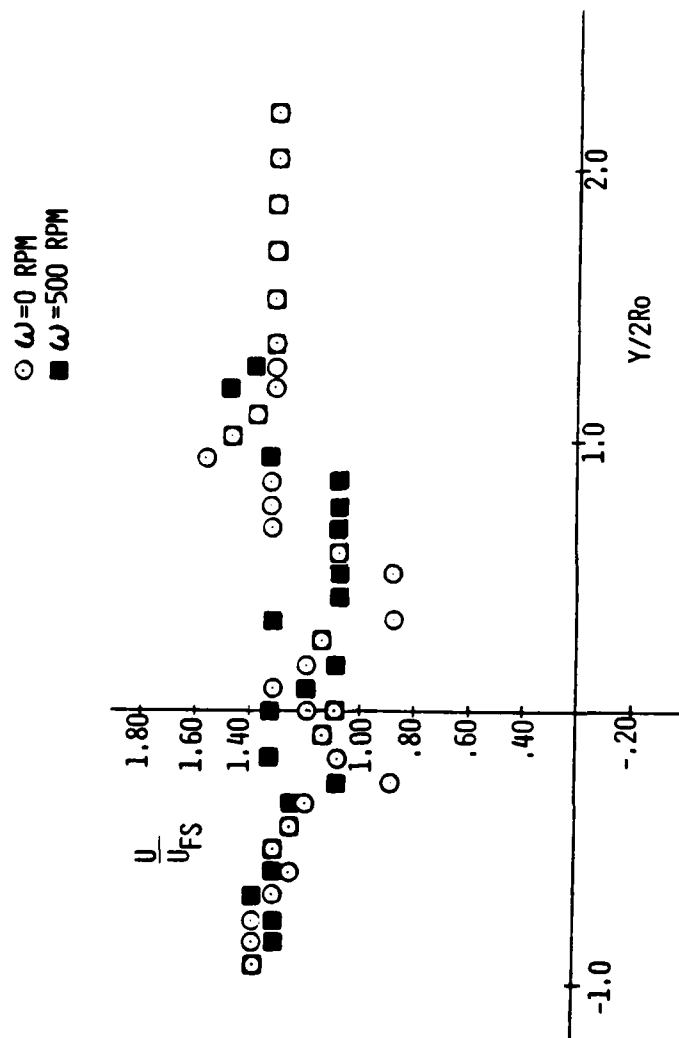


FIGURE 14. LATERAL MEAN VELOCITY PROFILE, $X/2R_o=2.0$

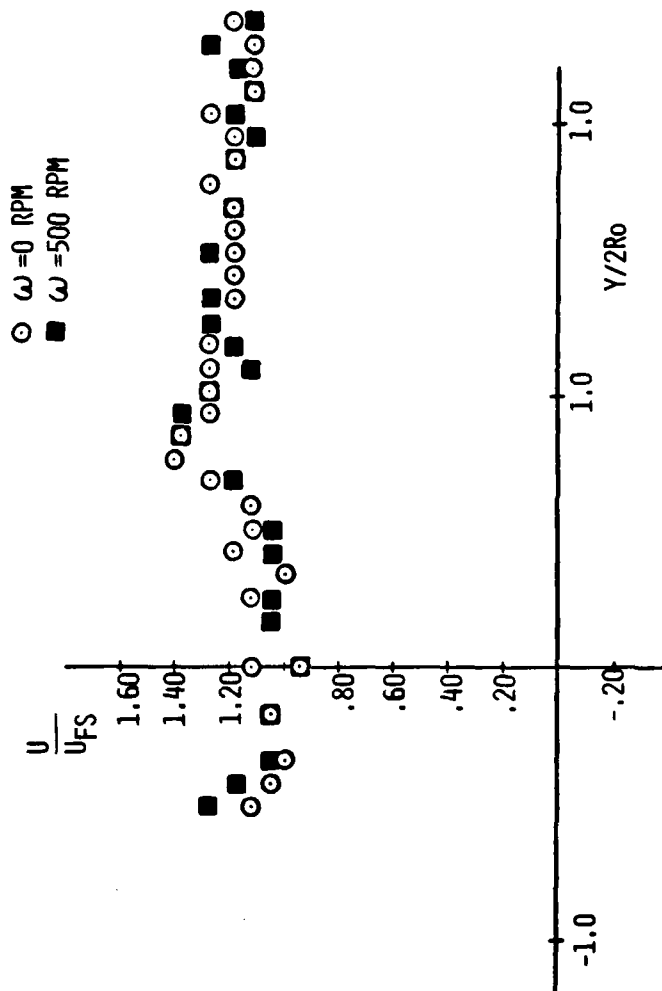


FIGURE 15. LATERAL MEAN VELOCITY PROFILE, $X/2R_0=3.0$

○ $\omega = 0$ RPM
 ■ $\omega = 500$ RPM

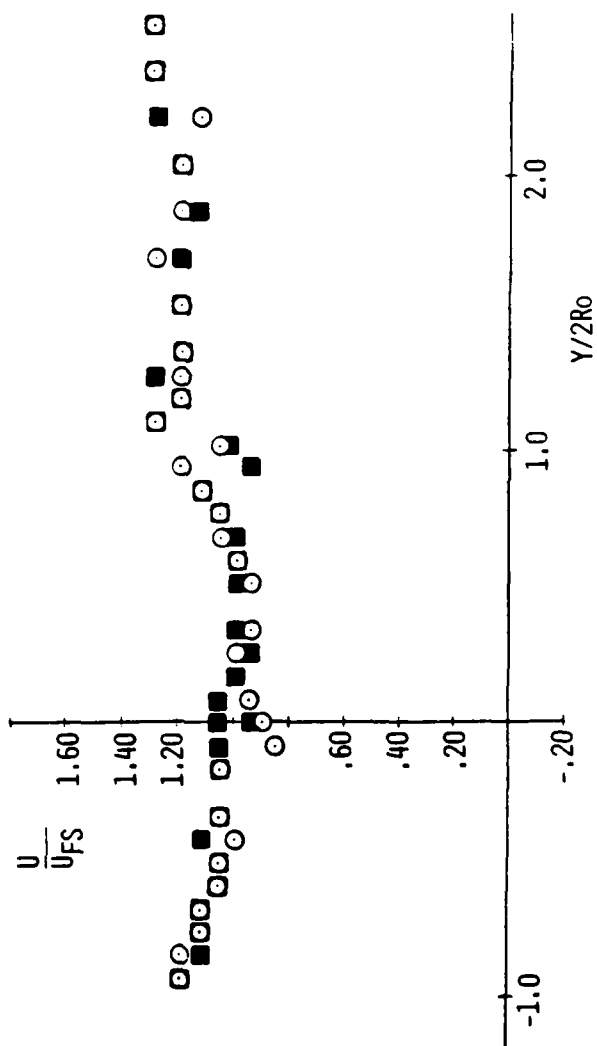


FIGURE 16. LATERAL MEAN VELOCITY PROFILE, $X/2R_o = 5.0$

(Figure 13). Observe that large velocity gradients ($\partial U/\partial Y$) exist at the boundaries of the recirculating region. The local mean velocities just outside of the recirculating region exhibit values in excess of freestream (i.e. $U/U_{FS} > 1.0$). This is attributed to the fact that the flow has experienced an acceleration and then deceleration in traversing around the cylinder. The deceleration to U_{FS} with downstream location ($U/U_{FS} \approx 1.4$ at $X/2Ro = 0.0$, whereas $U/U_{FS} \approx 1.2$ at $X/2Ro = 0.50$) in the area of the recirculating region is not complete. Effects of cylinder rotation at $\omega = 500$ RPM on mean velocities are noted as being negligible in the recirculating region.

At further downstream locations ($X/2Ro = 0.75$ to $X/2Ro = 5.00$ or Figures 12 to 16) note that the profile velocity deficit $(U_{MAX} - U_{LOCAL})/U_{FS}$ decreases in the downstream direction and the wake width appears to be growing. Figure 17 addresses the apparent growth of the wake half width. Wake half width is defined as:

$$Y_M = \frac{(U/U_{FS})_{MAX} - (U/U_{FS})_{CENTERLINE}}{2}$$

It is nondimensionalized by the cylinder radius and plotted versus the downstream location nondimensionalized by twice the cylinder radius. Neglecting the data between $X/2Ro = 0.0$ and $X/2Ro = 2.00$ (dashed line) it appears that the wake half width is growing at a rate of approximately 5 degrees.

At the downstream locations $X/2Ro = 2.0$ and $X/2Ro = 3.0$ note the existence of a region of higher velocity flow at the centerline of the wake and of lower velocity flow on either side of the centerline. This feature is more distinct at $X/2Ro = 2.0$ than $X/2Ro = 3.0$. Therefore, it appears to be decaying with downstream location. Consideration of

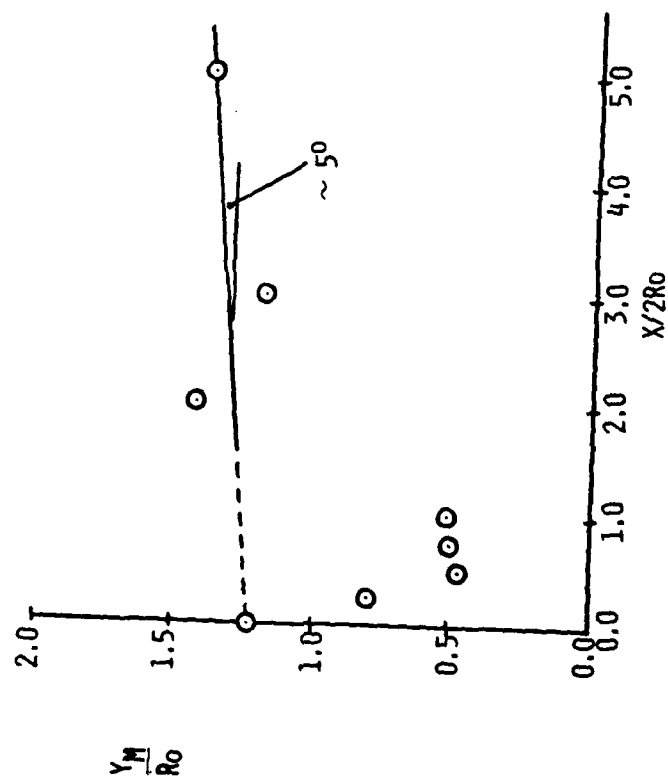


FIGURE 17. WAKE HALF WIDTH GROWTH

location $X/2Ro=5.0$ (Figure 16) reveals that this is the case. This behavior will be discussed in more detail when variation of centerline velocity is treated.

Returning again to the effects of cylinder rotation on the mean velocities, a scan of the mean velocity profiles downstream of the recirculating region (Figures 12 to 16) reveal that rotation at $\omega=500$ RPM has no effect here, as was also the case in the recirculating region.

The development of centerline mean velocities downstream is shown in Figure 18. Note the recirculating region with its reverse flow and the immediately following steep velocity gradient. The return to free-stream velocities (dashed line) at centerline is rapid (within $X/2Ro=4.00$) as expected in flow with a low freestream velocity of 5.9 m/sec. A slight overshoot in centerline velocity occurs between $X/2Ro=1.00$ and $X/2Ro=3.00$, followed by an asymptotic decay to free-stream values.

One of the parameters of interest in this investigation is the effect of cylinder rotation rates on the mean velocities in the cylinder flowfield. The preceeding discussion revealed the lack of effect of rotation on the cylinder near wake. Further evidence of this is provided in Figure 19. The location $X/2Ro=0.0$, $Y/2Ro=0.34$ is in the cylinder recirculating region. For values of ω from 0 to 800 RPM no significant change in U/U_{FS} is noted. Also in Figure 19 the effect of rotation for location $X/2Ro=0.75$, $Y/2Ro=0.6$ is presented. This location is considered to be significant, because it is located outside of the recirculating region and in the region of vortex formation. The effect of rotation is again insignificant.

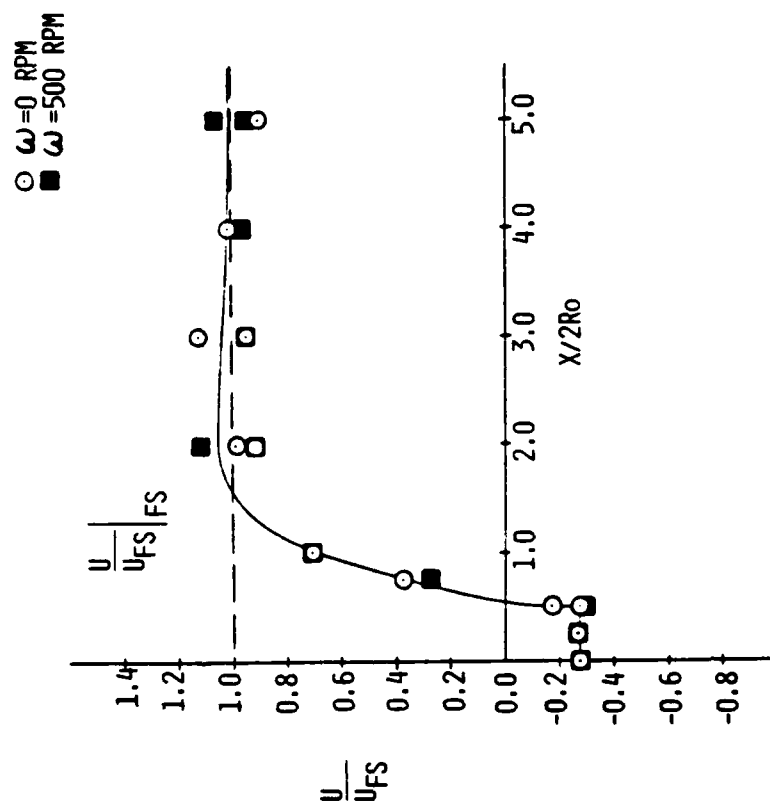


FIGURE 18. DEVELOPMENT OF CENTERLINE MEAN VELOCITY PROFILE

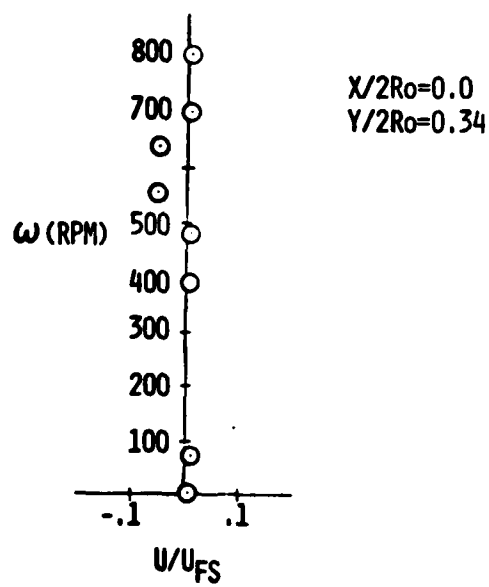
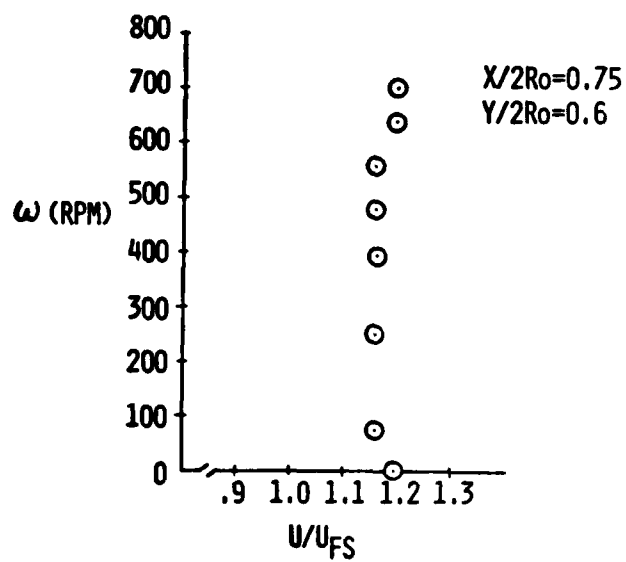


FIGURE 19. EFFECT OF CYLINDER ROTATION ON MEAN VELOCITIES

The effect of rotation on the mean velocities outside of the near wake and in a region of potential flow is shown in Figure 20. A lateral traverse in the positive $Y/2R_o$ direction is shown for $X/2R_o = -0.50$. According to potential flow theory at $\theta = 90$ degrees, the local velocity should increase as the cylinder surface is approached radially according to

$$U = U_{FS} \left(1 + \frac{A^2}{R_o^2} \right)$$

until a value of $2 U_{FS}$ is reached at $A = R_o$, $\theta = 90$ degrees (the cylinder surface). Agreement between the potential flow theory and the measured mean velocities at $\omega = 0$ RPM is reasonable. With $\omega = 500$ and rotating clockwise an increase in local mean velocities is noted from the surface ($Y/2R_o = 0.5$) out to $Y/2R_o = 1.36$. Reversing the direction of rotation (from clockwise to counterclockwise) produces lower local mean velocities out to $Y/2R_o = 1.36$. It would appear then, that the effects of rotation on mean velocities are most significant in potential flow regions close to the cylinder surface. Flow acceleration around the cylinder is again in evidence (at $X/2R_o = -0.5$) by the return of U/U_{FS} to values above 1.0 for lateral positions increasing outward from the cylinder. The ability of the laser doppler velocimeter to define the cylinder boundary layer is shown by the rapid decrease in mean velocity from $U/U_{FS} = 1.8$ to $U/U_{FS} = 0.0$ in a $\Delta Y/2R_o$ of 0.045. This corresponds to a boundary layer thickness of slightly over one half of a centimeter.

A second parameter of interest was the effect of marker particle concentrations on mean velocity measurements. High levels of marker particle concentration can result in two phase flows, creating a flow-field different from the desired one. Marker particle concentrations

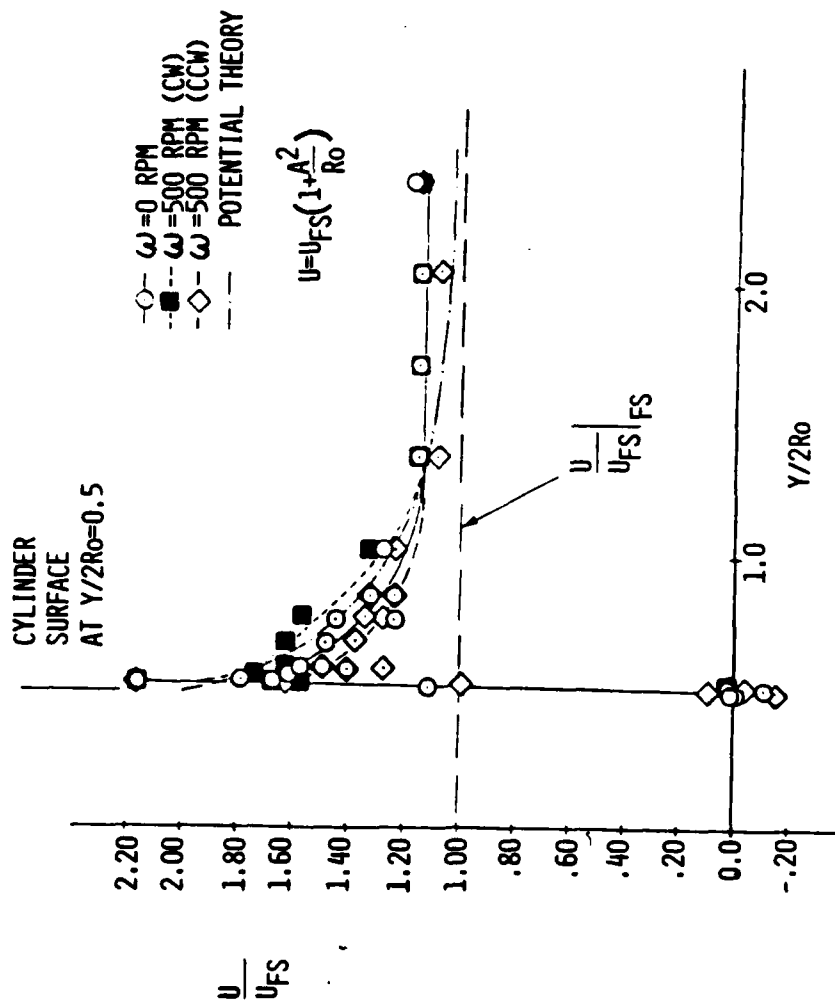


FIGURE 20. EFFECT OF CYLINDER ROTATION ON MEAN VELOCITIES,
 $X/2R_o = -0.5$

were not qualitatively determined in this investigation. It was deemed sufficient to visually observe the intensity of scattered laser beam light coming from the control volume and assume that higher intensities indicate higher concentrations. Actually, the relation between visual observation and intensity is a logarithmic one. The calculated mean velocities and turbulent intensities (Appendix A) based upon this concentration study are presented in Table II.

MARKER PARTICLE CONCENTRATION LEVEL	U/U_{FS}	U_{RMS}/U_{FS}
1 (low)	0.99	0.15
2	1.05	--
3	0.94	0.14
4 (high)	0.94	0.15

TABLE II Effect of Marker Particle Concentration on Mean Velocities and Turbulent Intensities at $X/2Ro=5.00$, $Y/2Ro=0.0$.

Any deviations are within the experimental error (approximately 5 percent) and the concentration levels in use are assumed to produce no two phase flow effects.

A factor that greatly affects the reliability of laser doppler velocimeter measurements is the size of the pinhole diameter in the detector system. Three pinhole diameters are available for study (100 μm , 200 μm and 400 μm). The effect, on mean velocities in two differing flowfield regions, of pinhole diameter was studied. Table III a presents results taken in the cylinder recirculating region at $X/2Ro=0.50$, $Y/2Ro=0.0$. U/U_{FS} values are unchanged with varying pinhole diameter. Tables III b and III c present results in the flowfield region upstream of the cylinder (free stream). Any variations detected in U/U_{FS}

PINHOLE DIAMETER (μM)	U/U_{FS}	U_{RMS}/U_{FS}
100	- 0.27	1.27
200	- 0.27	2.24
400	- 0.27	0.46

A. $X/2R_o=0.50$, $Y/2R_o=0.0$

PINHOLE DIAMETER (μM)	U/U_{FS}	U_{RMS}/U_{FS}
100	0.95	0.08
400	0.89	0.22

B. $X/2R_o=-2.65$, $Y/2R_o=0.13$

PINHOLE DIAMETER (μM)	U/U_{FS}	U_{RMS}/U_{FS}
100	1.00	0.04
200	1.00	--
400	1.00	0.15

C. $X/2R_o=-2.13$, $Y/2R_o=-0.09$

TABLE III EFFECT OF PINHOLE DIAMETER ON MEAN VELOCITIES
AND TURBULENT INTENSITIES

approach the value of the experimental error (approximately 5%).

Finally, little information exists on the effect of frequency shifting on turbulence measurements (Reference 7). In this investigation regions of very high turbulence (greater than 30%) were encountered, which necessitated the use of the frequency shifting crystal oscillator. A study was made to determine the effect on mean velocities of this shifting and the results are presented in Figure 21. The cylinder recirculating region and several locations upstream of the cylinder were probed. Mean velocities are plotted versus the amount of frequency shift in KHz. Both regions exhibit a nonlinear trend with increasing shift. Frequency shifts employed in the freestream region ahead of the cylinder of up to 20 KHz appear to be correct, since the values of U/U_{FS} nonshifted and U/U_{FS} shifted are both close to 1.0. In the cylinder recirculation region shifts of from 200 KHz to 800 KHz appear to produce results that are more in agreement with the low negative velocities expected. The vast majority of measurements taken in this investigation, when the frequency shifting was required, were at 200 KHz.

Turbulent Intensities

Turbulent intensity is defined as the ratio of the root mean square of the turbulent velocity fluctuations to a reference mean velocity. In this investigation the reference mean velocity is the free stream velocity. Therefore,

$$\text{Turbulent intensity} = U_{RMS}/U_{FS}$$

where:
$$U_{RMS} = \left[\frac{1}{T} \int_0^T U'^2 dt \right]^{1/2}$$

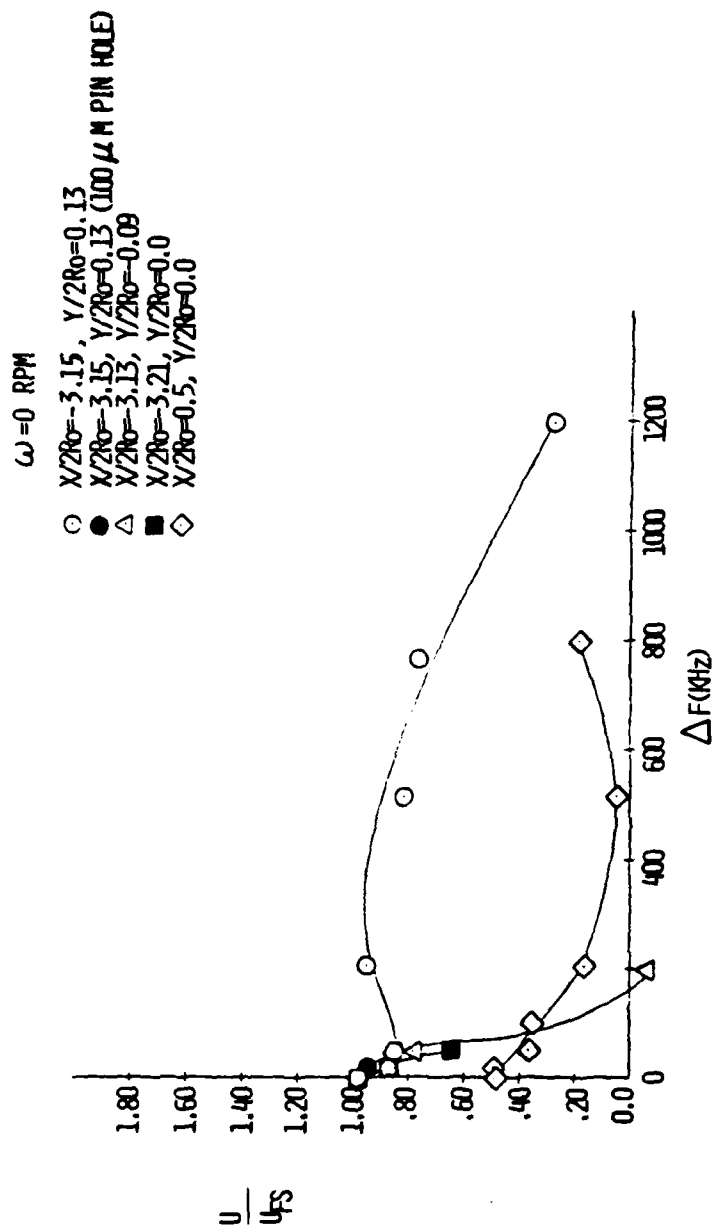


FIGURE 21. EFFECT OF DOPPLER SHIFT ON MEAN VELOCITIES

All turbulent intensity measurements have been corrected for ambiguity noise. Ambiguity noise is defined as an apparent turbulence resulting from the finite transit times of marking particles as they pass through the control volume fringes in a random manner. It is a direct result of the finite size of the laser measuring volume (Appendix C). This correction, which is a constant for the investigation optical setup, is subtracted from the computed turbulent intensities. Its value was determined to be 0.039 or 3.9%. Accuracy of turbulent intensity measurements is approximately 5%, since it is computed as U_{RMS}/U_{LOCAL} and U_{LOCAL} is accurate to within 5%.

Lateral profiles of turbulent intensity are presented in Figures 22 to 29 for downstream locations $X/2Ro=0.0, 0.25, 0.50, 0.75, 1.00, 2.00, 3.00$ and 5.00 , with the cylinder both rotating and nonrotating. The lateral displacement from the flow centerline is again nondimensionalized by twice the cylinder radius. At $X/2Ro=0.0$ (Figure 22) note the higher turbulent intensity at the centerline and the inclusion of the majority of data between turbulent intensity values of 0.10 and 0.30 (10% and 30% respectively). Values of turbulent intensity at locations upstream of the cylinder were typically on the order of 0.10 (based on an average of several measurements). Progressing downstream in the cylinder recirculation region to $X/2Ro=0.25, 0.50$ and 0.75 extremely high turbulent intensities are encountered. Turbulent intensity values computed to be in excess of 100% are not plotted. Instead a perceived trend (for the $\omega=0$ RPM case) to higher values is indicated by dashed lines. The trends are symmetrical about the centerline. Upon comparison with mean velocity profiles at the same $X/2Ro$ locations (Figures 9 to 16), it becomes apparent that, the lateral positions ($Y/2Ro$) of the high

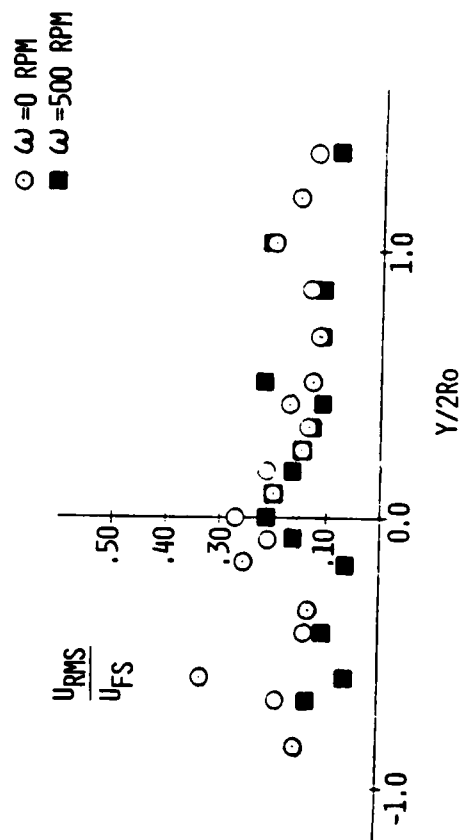


FIGURE 22. LATERAL TURBULENT INTENSITY PROFILE, $X/2R_o=0.0$

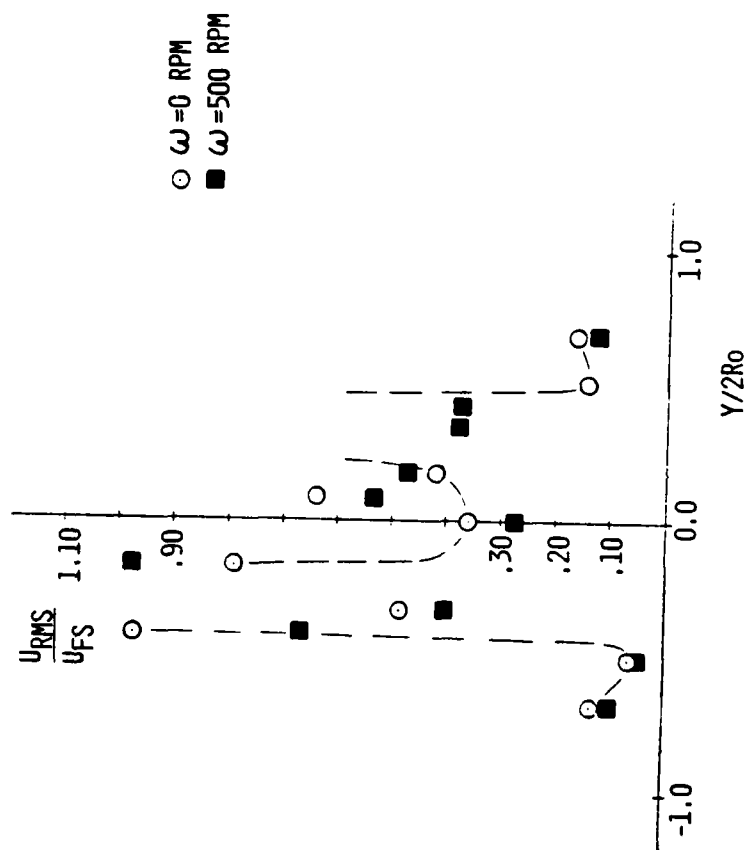


FIGURE 23. LATERAL TURBULENT INTENSITY PROFILE,
 $X/2R_0=0.25$

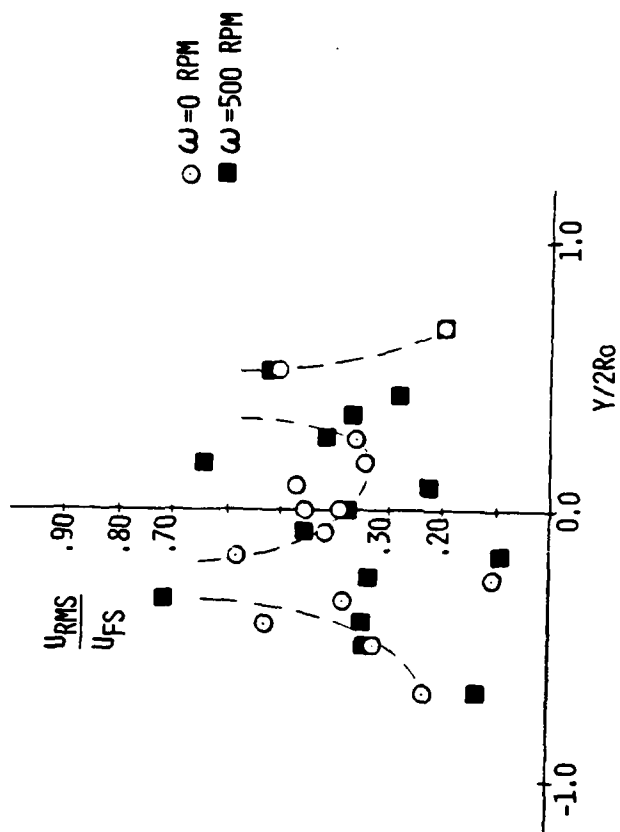


FIGURE 24. LATERAL TURBULENT INTENSITY PROFILE,
 $X/2R_0=0.5$

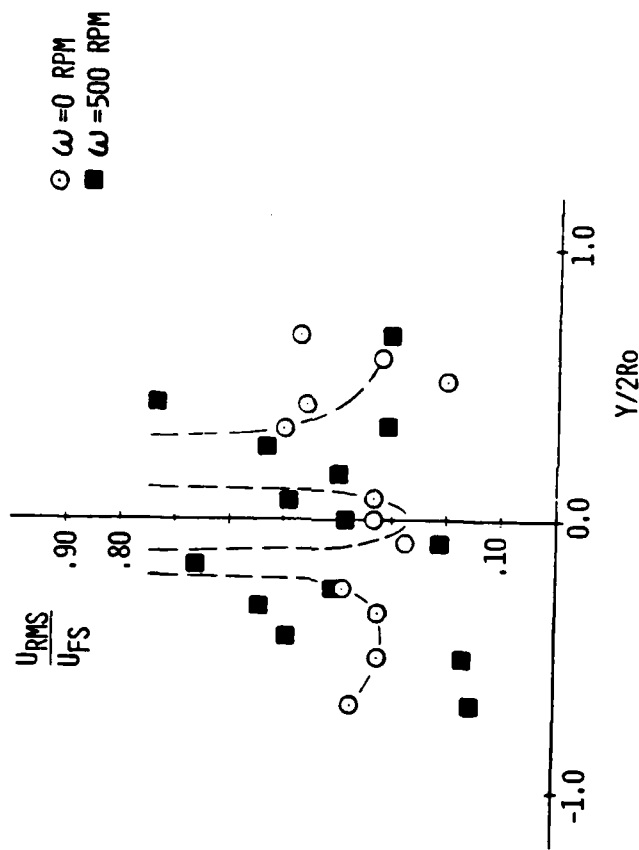


FIGURE 25. LATERAL TURBULENT INTENSITY PROFILE,
 $X/2R_0=0.75$

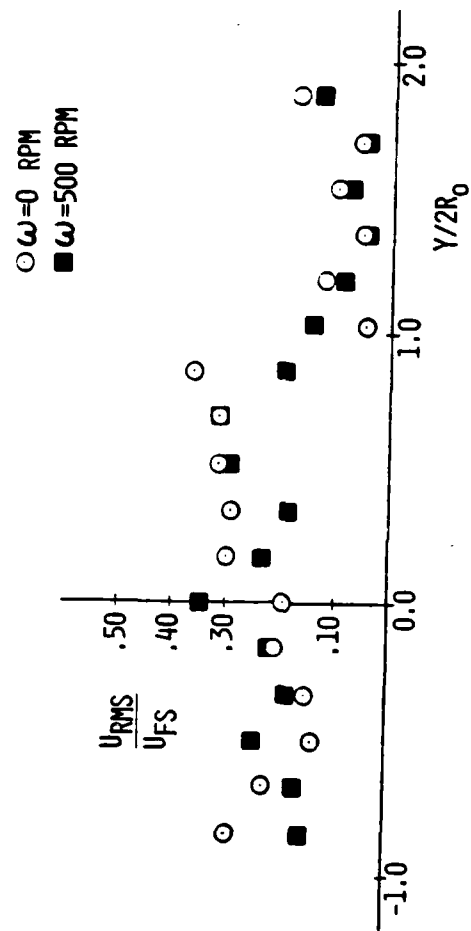


FIGURE 26. LATERAL TURBULENT INTENSITY PROFILE, $X/2R_0=1.0$

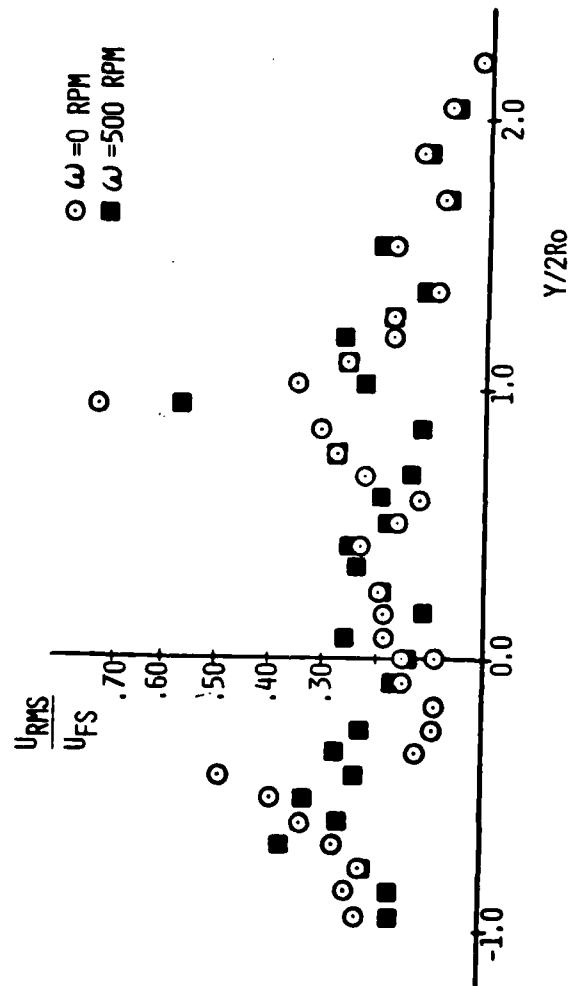


FIGURE 27. LATERAL TURBULENT INTENSITY PROFILE, $X/2R_o=2.0$

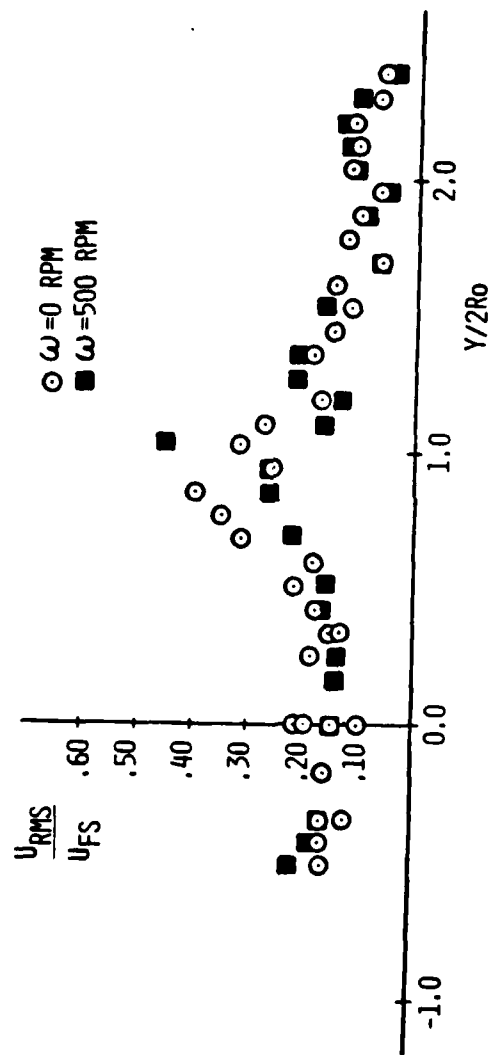


FIGURE 28. LATERAL TURBULENT INTENSITY PROFILE, $X/2R_0=3.0$

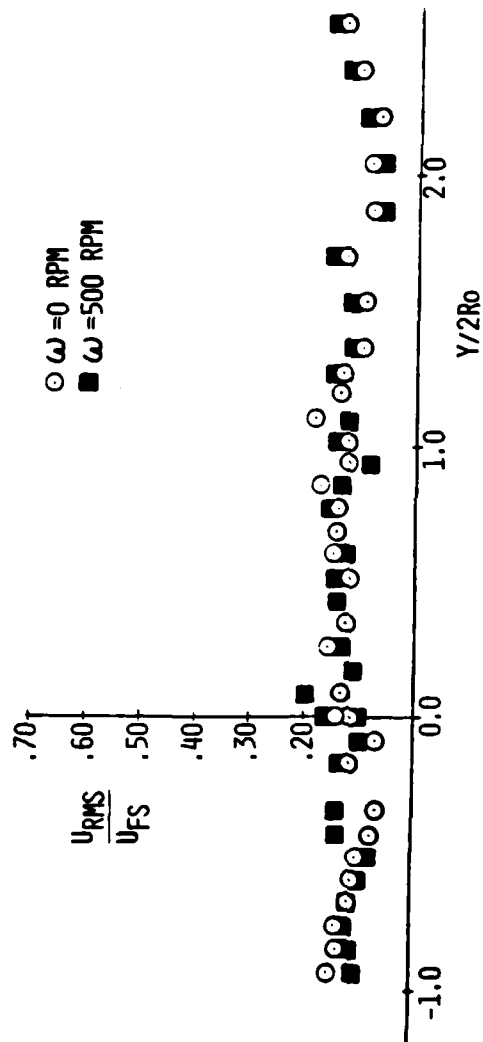


FIGURE 29. LATERAL TURBULENT INTENSITY PROFILE, $X/2R_0=5.0$

mean velocity gradients match the lateral positions of the high turbulent intensities. Consider that the transfer term in the equation for the kinetic energy of mean motion (Reference 8)

$$\rho \overline{U' V'} \frac{\partial U}{\partial Y}$$

represents the exchange of energy from the mean flowfield to the turbulent flowfield by the interaction of Reynolds' stresses ($\rho \overline{U' V'}$) with the mean velocity gradient ($\partial U / \partial Y$). In this investigation the Reynolds' stresses are unknown, but the mean velocity gradient is known. The fact that the mean velocity gradient is large indicates that a substantial transfer of energy is taking place from the mean flowfield to the turbulent flowfield. Therefore, large turbulent intensities are to be expected in regions of high mean velocity gradients.

The scatter in the turbulent intensity data in the recirculating region for a cylinder rotation rate of $\omega=500$ RPM is difficult to define due to the large gradients. In regions of lower gradients the scatter appears to be on the order of 10%. The only conclusion that can be reasonably drawn, as regards the effects of rotation, is that the excessive turbulent intensities ($>100\%$) observed for the $\omega=0$ RPM case are not observed in the $\omega=500$ RPM case.

Moving downstream from $X/2Ro=1.00$ to $X/2Ro=5.00$ (Figures 26 to 29), it is still the case that regions of highest turbulent intensity correspond to regions of highest mean velocity gradients. The peak magnitudes observed in the recirculating region are not repeated here, but are still significantly above free stream values ($U_{RMS}/U_{FS}=0.10$). By the time location $X/2Ro=5.00$ is reached the turbulent intensities have returned to near free stream values. A check of the mean velocity

gradients at $X/2R_o=5.00$ (Figure 29) reveals a substantial reduction in their magnitude signalling a reduction in peak turbulent intensities as well.

The effects of cylinder rotation downstream of the cylinder recirculating region appear to be confined to a reduction in peak magnitudes as was also the case in the recirculating region.

The development of centerline turbulent intensities downstream is shown in Figure 30. An additional effect of cylinder rotation now comes to light. In the recirculation region and up to $X/2R_o=2.00$ a shift in the location of peak turbulent intensity occurs from $X/2R_o=0.50$ to $X/2R_o=0.75$. In addition there is a broadening of the curve between $X/2R_o=0.00$ and $X/2R_o=2.00$ indicating a growth of the region of higher turbulent intensities downstream. A rapid return toward free stream values is noted beginning at $X/2R_o=2.00$. The effects of rotation from $X/2R_o=2.00$ on downstream are negligible.

As stated previously one parameter of interest was the effect of varying cylinder rotation rates (ω) on turbulent measurements. The effect of rotation on turbulent intensities at two differing locations is shown in Figure 31. At $X/2R_o=0.0$, $Y/2R_o=0.34$ (the recirculating region) an increase in clockwise ω produces a decrease in turbulent intensities up to $\omega=800$ RPM. This agrees with the early observations of Prandtl (Reference 9).

This result corresponds well with that observed in Figure 22 for $X/2R_o=0.0$ and $\omega=500$ RPM. At $X/2R_o=0.75$, $Y/2R_o=0.6$ (region of shed vortex formation) the effect of increasing ω is again one of initial decrease in turbulent intensity accompanied by an increase toward $\omega=0$ RPM values of turbulent intensity at $\omega=700$ RPM. This effect has

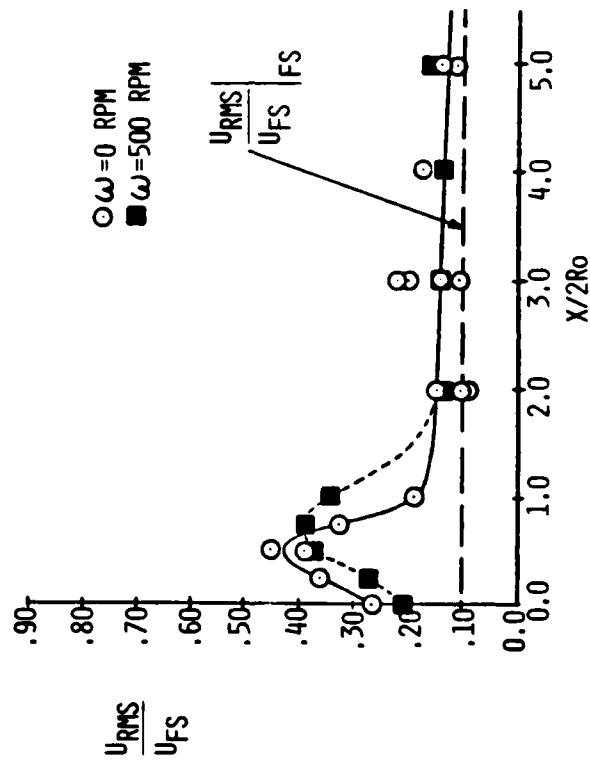


FIGURE 30. DEVELOPMENT OF CENTERLINE TURBULENT INTENSITY PROFILE

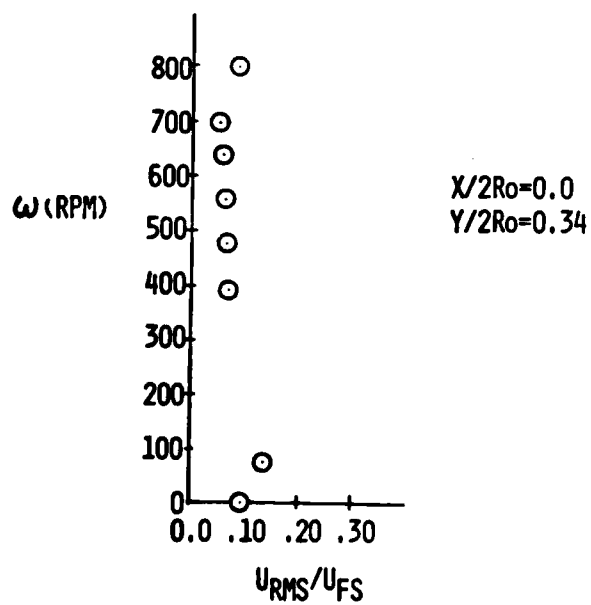
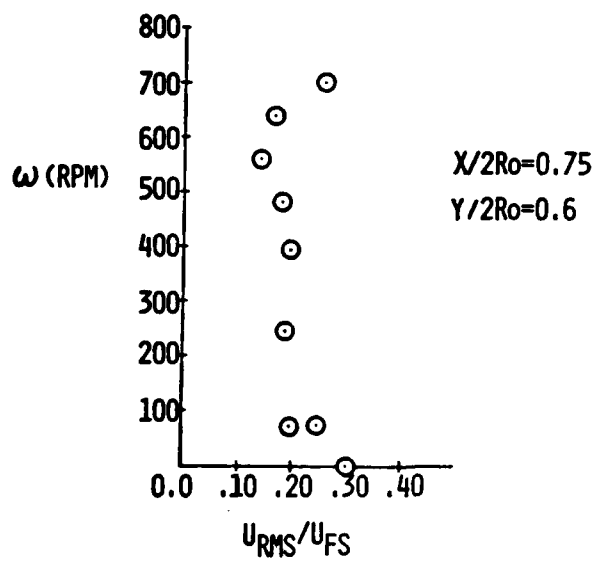


FIGURE 31. EFFECT OF CYLINDER ROTATION ON TURBULENT INTENSITIES

been observed in other work with rotating shapes (Reference 10). It is then apparent that, in the near wake region of the circular cylinder, rotation has insignificant effects upon mean velocities, but has pronounced effect upon turbulent intensities. Returning to the potential flow region above the cylinder ($\theta=90$ degrees), the lateral variation of turbulent intensity is presented in Figure 32. Effects of rotation lie within experimental error and are therefore ignored. Rotational effects outside of the boundary layer are insignificant. Note that free stream values of turbulent intensity are indicated by the dashed line.

The effect of marker particle concentrations on turbulent intensities at $X/2R_o=5.00$, $Y/2R_o=0.0$ are presented in Table II. Turbulent intensity values at concentration level 2 are undefined. As with the mean velocities, no effects of concentration levels are noted on turbulent intensities.

Pinhole diameter sizes have a pronounced effect on turbulent intensity measurements as shown in Table III. In the recirculating region ($X/2R_o=0.50$, $Y/2R_o=0.0$) the smaller pinhole diameters (100 μm and 200 μm) give values of turbulent intensity in excess of 100%, whereas, in the freestream locations $X/2R_o=-2.65$, $Y/2R_o=0.13$ and $X/2R_o=-2.13$, $Y/2R_o=-0.09$ they give smaller turbulent intensities than the 400 μm diameter pinhole. With smaller pinhole diameters, fewer marker particles are sensed as they traverse the control volume fringes. This results in a low signal to noise ratio entering the photon correlator. To the correlator the signal appears as white noise. An autocorrelation of white noise appears as a spike at $T=0.0$ (zero time of averaging) resulting in large turbulent intensity values. In the recirculation region, where fewer particles would be expected to traverse the fringe

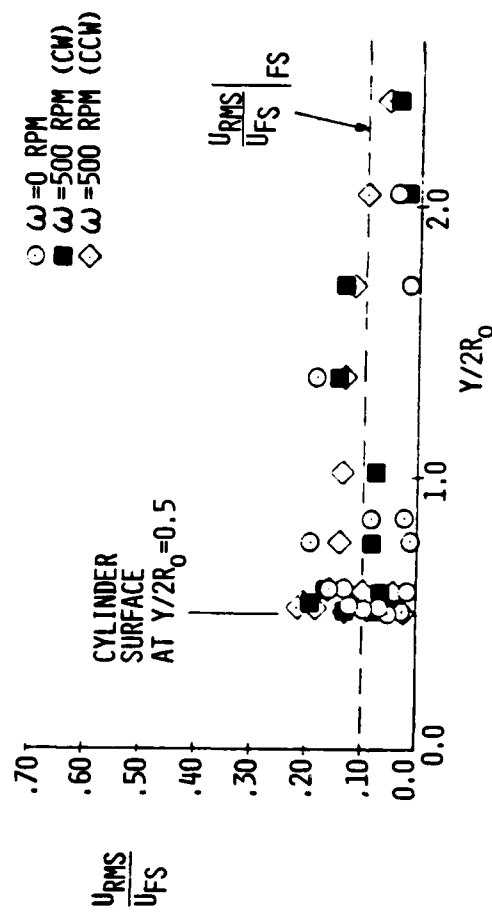


FIGURE 32. EFFECT OF CYLINDER ROTATION ON TURBULENT INTENSITIES
 $X/2R_0 = -0.5$

pattern, high turbulent intensities would be computed. This phenomena does not explain the decrease in turbulent intensity with decrease in pinhole diameter observed in the freestream. Further study of pinhole diameter effects in the freestream is required to more accurately define the causes of this anomaly. Other measurements of turbulent intensities in the freestream, with the 400 μm diameter pinhole resulted in values of $U_{\text{RMS}}/U_{\text{FS}}$ of 0.13, 0.11, 0.03 and -0.02. The results appear to be dependent on the positioning of the control volume in the streamtubes issuing from the stack/injector system. An average value of $U_{\text{RMS}}/U_{\text{FS}}$ of 0.10 was assumed to be representative of the freestream.

Finally, frequency shift effects on turbulent intensities are shown in Figure 33. For the freestream measurements, which normally did not require frequency shifting, any applied shift of over 20 KHz gives results inconsistent with the efforts to reduce the tunnel turbulence levels (Reference 5). In the recirculation region, shifts below 200 KHz produced autocorrelation functions whose maxima and minima points were undetectable. Shifts above 200 KHz produce varying results. Since 200 KHz appeared to produce realistic mean velocity measurements, it is assumed that turbulent intensity measurements taken at a shift of 200 KHz are also acceptable. Further experimentation and analysis appears warranted in order to better define the effects of frequency shifting on turbulent measurements.

Integral Time Scales

Longitudinal integral time scales are defined as follows:

$$T_{\text{IS}} = \int_0^{T_{\text{CIS}}} U'(T)U'(T')dT'$$

$\omega = 0$ RPM
 \circ X/2Ro=-3.15, Y/2Ro=0.13
 \triangle X/2Ro=-3.13, Y/2Ro=-0.09
 \blacksquare X/2Ro=-3.21, Y/2Ro=0.0
 \diamond X/2Ro=0.5, Y/2Ro=0.0

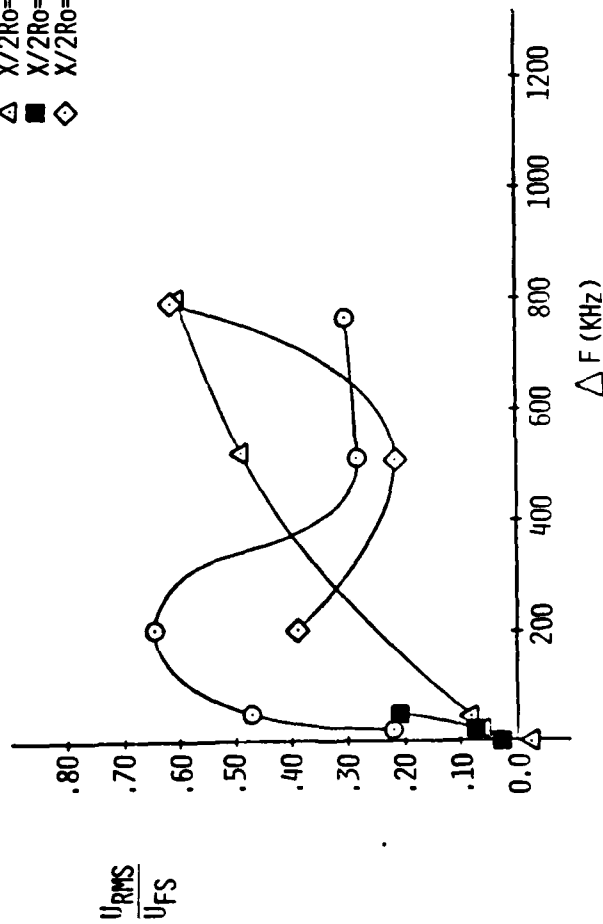


FIGURE 33. EFFECT OF DOPPLER SHIFT ON TURBULENT INTENSITIES

or
$$T_{IS} = \int_0^{T_{CIS}} R(T') dT'$$

where: $R(T')$ = autocorrelation function

T_{CIS} = time to first zero crossing of autocorrelation function

The integral in this definition represents the area under the autocorrelation function to its first zero crossing. This standard method of determining integral scales is departed from in this investigation. Details of the actual method employed are given in Appendix D.

Time scales are presented instead of length scales because Taylor's hypothesis

$$U \frac{d}{dx} (\bar{Q}) = \frac{d}{dt} (\bar{Q})$$

relating length scales to time scales cannot be realistically utilized in this investigation. The local mean velocity (U) is not constant and the statistical property \bar{Q} is not stationary for statistical equilibrium to exist.

Integral scales represent the largest turbulent scale in the flow-field. The development of integral time scales with downstream location, for various lateral positions ($Y/2R_o=0.0, 1.02, 2.04$ and -0.94) are presented in Figure 34 and a complete compilation is provided in Table IV. The method of determining the time scales (Appendix D) is an approximate technique, subject to large errors, as seen by the scatter in Figure 34. Ignoring points of large deviation, it is possible to construct a linear curve fit through all available data points. The resultant curve indicates a slow rate of increase in integral time scales with downstream location. Further observations concerning the data are not warranted

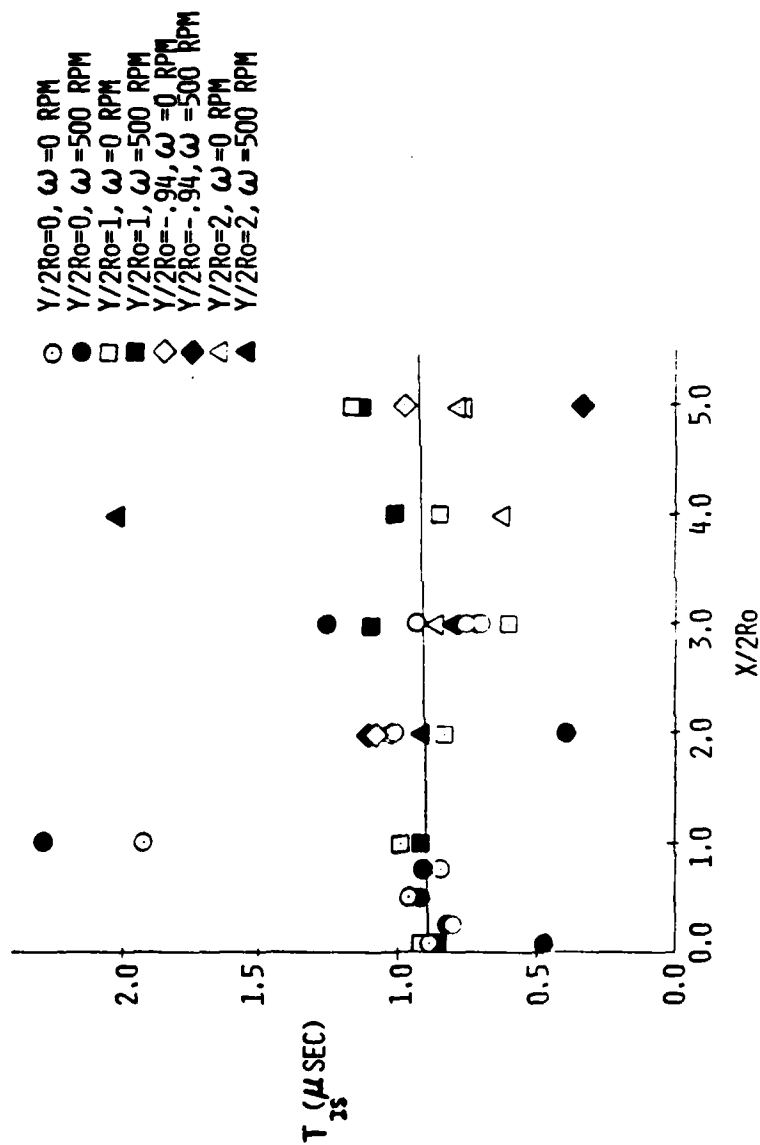


FIGURE 34. DEVELOPMENT OF LONGITUDINAL INTEGRAL TIME SCALES

X/2Ro	Y/2Ro=0.0		Y/2Ro=1.02		Y/2Ro=2.04		Y/2Ro=-0.94	
	$\omega=0$	$\omega=500$	$\omega=0$	$\omega=500$	$\omega=0$	$\omega=500$	$\omega=0$	$\omega=500$
0.0	$.89 \times 10^{-6}$ ^A	$.48 \times 10^{-6}$ ^A	$.92 \times 10^{-6}$	$.86 \times 10^{-6}$	$.98 \times 10^{-6}$ ^F	$.90 \times 10^{-6}$ ^F		
0.25	$.81 \times 10^{-6}$	$.82 \times 10^{-6}$						
	$.86 \times 10^{-6}$ ^B	$.96 \times 10^{-6}$ ^B						
0.50	1.08×10^{-6} ^C	1.13×10^{-6} ^C						
	$.96 \times 10^{-6}$	$.92 \times 10^{-6}$						
0.75	$.85 \times 10^{-6}$	$.92 \times 10^{-6}$						
1.00	1.92×10^{-6}	2.28×10^{-6}	$.99 \times 10^{-6}$	$.92 \times 10^{-6}$	1.13×10^{-6} ^G	1.01×10^{-6} ^G		
2.00	1.02×10^{-6}	$.41 \times 10^{-6}$	$.84 \times 10^{-6}$	$.84 \times 10^{-6}$	1.04×10^{-6}	$.92 \times 10^{-6}$	1.08×10^{-6}	1.12×10^{-6}
3.00	$.71 \times 10^{-6}$		$.61 \times 10^{-6}$	1.10×10^{-6}	$.84 \times 10^{-6}$	$.81 \times 10^{-6}$		
	$.94 \times 10^{-6}$	1.26×10^{-6}						
	$.76 \times 10^{-6}$	$.72 \times 10^{-6}$						
	$.80 \times 10^{-6}$ ^D	$.72 \times 10^{-6}$ ^D						
4.00			$.86 \times 10^{-6}$	1.02×10^{-6}	$.63 \times 10^{-6}$	2.03×10^{-6}		
5.00			1.18×10^{-6}	1.13×10^{-6}	$.77 \times 10^{-6}$	$.77 \times 10^{-6}$	$.98 \times 10^{-6}$	$.34 \times 10^{-6}$
		1.23×10^{-6} ^E			$.79 \times 10^{-6}$			

- A X/2Ro=0.09
 B X/2Ro=0.25, Y/2Ro=0.17
 C X/2Ro=0.25, Y/2Ro=-0.17
 D X/2Ro=3.00, Y/2Ro=0.09
 E X/2Ro=5.00, Y/2Ro=1.17
 F X/2Ro=-0.5, Y/2Ro=1.70
 G X/2Ro=1.00, Y/2Ro=1.87

TABLE IV INTEGRAL TIME SCALES

because of the approximate nature of the integral time scale method of determination.

Taylor Time Microscales

Taylor microscales are defined as the ratio of the dissipation of energy to the total amount of energy in the flow. They lie between the largest scales (integral scales) and the smallest scales (Kolmogorov scales). Their experimental determination is outlined in Appendix E. The centerline variation of Taylor time microscales with downstream location is addressed in Figure 35. A complete tabulation of variations with downstream location, for several lateral positions is given in Table V. Returning to Figure 35, if large deviation points are ignored, a curve can be fitted to the data that indicates a slight increase in Taylor time microscales downstream. The growth rate of this curve is approximately equal to that of the integral time scale. Cylinder rotation has no appreciable effect on this curve.

Kinetic Energy Dissipation Rates

The kinetic energy dissipation rate is proportional to the Taylor velocity microscale cubed, over the integral length scale (Reference 11):

$$\epsilon \sim \frac{U_{\lambda}^3}{L}$$

where: $U_{\lambda} = \frac{S}{T_{C_{MS}}}$

$$L = T_{IS} \times U$$

In order to calculate the kinetic energy dissipation rate, it is necessary to assume that the Taylor hypothesis holds. With this assumption made and recalling the approximate nature of the integral time scale

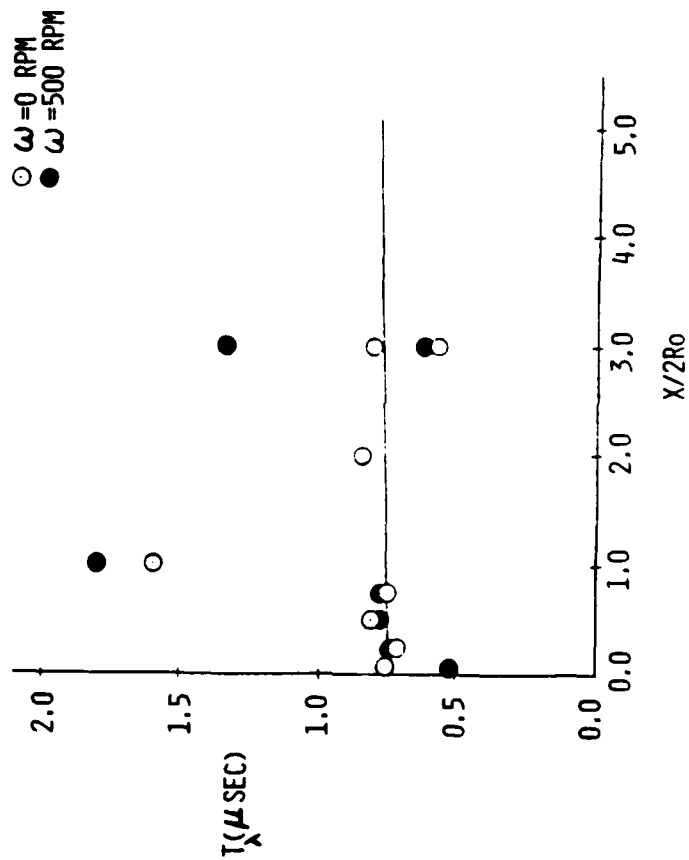


FIGURE 35. DEVELOPMENT OF LONGITUDINAL TAYLOR TIME MICROSCALES

X/2Ro	Y/2Ro=0.0		Y/2Ro=1.02		Y/2Ro=2.04		Y/2Ro=-0.94	
	$\omega = 0$	$\omega = 500$	$\omega = 0$	$\omega = 500$	$\omega = 0$	$\omega = 500$	$\omega = 0$	$\omega = 500$
0.0	$.76 \times 10^{-6}$ ^A	$.53 \times 10^{-6}$ ^A	$.75 \times 10^{-6}$	$.78 \times 10^{-6}$	$.81 \times 10^{-6}$ ^F	$.74 \times 10^{-6}$ ^F		
0.25	$.72 \times 10^{-6}$	$.74 \times 10^{-6}$						
	$.74 \times 10^{-6}$ ^B	$.79 \times 10^{-6}$ ^B						
	$.85 \times 10^{-6}$ ^C	$.92 \times 10^{-6}$ ^C						
0.50	$.82 \times 10^{-6}$	$.78 \times 10^{-6}$						
0.75	$.76 \times 10^{-6}$	$.78 \times 10^{-6}$						
1.00	1.60×10^{-6}	1.80×10^{-6}	$.84 \times 10^{-6}$	$.84 \times 10^{-6}$	$.83 \times 10^{-6}$ ^G	$.84 \times 10^{-6}$		
2.00	$.86 \times 10^{-6}$		$.69 \times 10^{-6}$		$.83 \times 10^{-6}$	$.76 \times 10^{-6}$	$.92 \times 10^{-6}$	$.88 \times 10^{-6}$
3.00	$.45 \times 10^{-6}$		$.72 \times 10^{-6}$		$.75 \times 10^{-6}$	$.77 \times 10^{-6}$		
	$.82 \times 10^{-6}$	1.35×10^{-6}						
	$.59 \times 10^{-6}$	$.64 \times 10^{-6}$						
	$.55 \times 10^{-6}$ ^D	$.58 \times 10^{-6}$ ^D						
4.00			$.84 \times 10^{-6}$	1.04×10^{-6}	$.46 \times 10^{-6}$	$.86 \times 10^{-6}$		
5.00		1.05×10^{-6} ^E	$.84 \times 10^{-6}$	$.92 \times 10^{-6}$	$.70 \times 10^{-6}$	$.75 \times 10^{-6}$	$.83 \times 10^{-6}$	$.53 \times 10^{-6}$

A X/2Ro=0.09

B X/2Ro=0.25, Y/2Ro=0.17

C X/2Ro=0.25, Y/2Ro=-0.17

D X/2Ro=3.00, Y/2Ro=0.09

E X/2Ro=5.00, Y/2Ro=0.17

F X/2Ro=-0.5, Y/2Ro=1.70

G X/2Ro=1.00, Y/2Ro=1.87

TABLE V TAYLOR TIME MICROSCALES

(T_{IS}) calculations, Figure 36 is presented for consideration. Energy dissipation rates are highest in the recirculating region. They drop to essentially zero at $X/2Ro=1.00$ and then gradually increase downstream. This trend provides further confirmation of the fact that, large transfers of energy from the mean flow to the turbulent flow are taking place at high rates in the recirculation region. Finally, cylinder rotation at $\omega=500$ RPM increases the rate of energy transfer in the recirculating region.

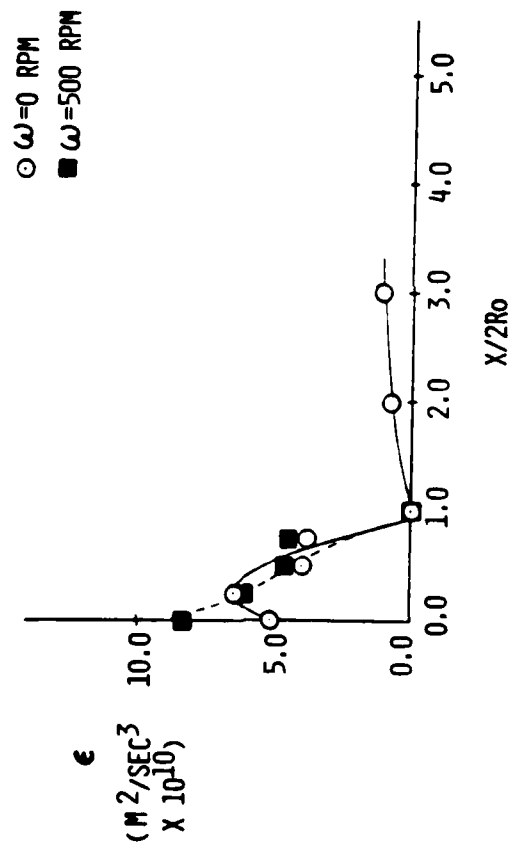


FIGURE 36. DEVELOPMENT OF CENTERLINE KINETIC ENERGY DISSIPATION RATES

IV CONCLUSIONS

The primary objective of this investigation is to determine how well the photon correlation/laser velocimeter system performed in the seeded flow environment of a two dimensional smoke tunnel. Several parametric studies were conducted to evaluate this performance and the conclusions resulting from them are listed below.

(1) Marker particle concentration ranges used in this investigation have no appreciable effect on local mean velocities or turbulent intensities.

(2) Pinhole diameters must be correctly chosen for the flowfield under study. Small pinhole diameters produce incorrect turbulent intensity data in regions of low velocity (e.g. recirculation regions behind cylinders). Recall that this is a consequence of the apparent fewer number of particles traversing the control volume fringes. In the freestream, turbulent intensity data with varying pinhole diameters is ambiguous and represents an incompatibility between the smoke injection method and the laser velocimeter system. Further study of this ambiguity is warranted. Mean velocity measurements are not affected by pinhole diameter.

(3) The effects of frequency shifting in recirculating regions or freestream regions requires further study.

(4) Particle lag in this investigation is negligible.

Conclusions not directly related to the primary objective, concern the nature of the circular cylinder flowfield and can be stated as follows.

(1) Cylinder rotation effects on the near wake (including recirculation region) are confined to influencing turbulent intensities.

Mean velocity effects are insignificant. In the potential flow regions of the cylinder flowfield the opposite trend is noted. Mean velocities are affected and turbulent intensities are unaffected.

(2) The integral time scales are larger than the Taylor time microscales as expected. Both time scales grow slowly downstream. The fact that their magnitudes are similar indicates that the energy containing region and dissipation region of the flow energy spectrum are not very far apart.

(3) High rates of energy transfer from the mean flow to the turbulent flow are taking place within the cylinder recirculation region. Observed frequencies of the integral scale and Taylor microscale were on the order of 100 KHz to 200 KHz, indicating small scale turbulent structures that are dissipative of energy.

Based upon this set of conclusions, it appears that the laser velocimeter system and the two dimensional smoke tunnel are highly complementary of each other, but further work is required in the interpretation of results from pinhole diameter effects and frequency shift effects.

V RECOMMENDATIONS

The following recommendations are advanced to improve the quality of investigations performed with the laser velocimeter/smoke tunnel system and to serve as a basis for future investigations with the same system.

(1) A more uniform method of introducing marker particles into the flow is required that would lower freestream turbulent intensities and make measurements in the freestream independent of position of the laser control volume.

(2) A traversing table should be designed and fabricated that allows the laser velocimeter to be run in the forward scatter mode for this flow facility.

(3) The electronic data processing should be upgraded to eliminate the time consuming hand recording of data.

(4) Smaller diameter cylinders should be tested that allow measurements to be taken in the far field wake for comparison with theory and prior empirical results.

(5) The parametric studies begun in this investigation should be expanded to include further values of U_{FS} , ΔF , marker particle concentration and ω . Pinhole diameter effects with the existing pinholes should be studied in greater detail at different flowfield locations.

(6) The scope of this investigation should be broadened by making measurements of power spectral densities, intermittencies, convection velocities, coherence of the velocity flowfield and pressure/velocity cross correlations.

BIBLIOGRAPHY

1. Cerrullo, N. G., An Experimental Evaluation of Laser Velocimetry by the Study of Turbulence in a Plane Free Jet at High Subsonic Velocities, M. S. Thesis, Wright-Patterson Air Force Base, Ohio: Air Force Institute of Technology (January 1979)
2. Rogers, H. J. V., Velocity Profiles in a Long Inlet Duct Employing a Photon Laser Velocimeter Without Seeding, M. S. Thesis, Wright-Patterson Air Force Base, Ohio: Air Force Institute of Technology (December 1979)
3. Krawtz, J. A., Ground Plane Effects on a Contoured Surface at Low Subsonic Velocities, M. S. Thesis, Wright-Patterson Air Force Base, Ohio: Air Force Institute of Technology (December 1979)
4. Morris, S. L., A Diagnostic Study of Flow in the Wake of a Circular Disk Using a Photon Correlation Laser Velocimeter, M. S. Thesis, Wright-Patterson Air Force Base, Ohio: Air Force Institute of Technology (January 1980)
5. Baldner, J. L., Completion of The Development of the AFIT Smoke Tunnel, M. S. Thesis, Wright-Patterson Air Force Base, Ohio: Air Force Institute of Technology (August 1959)
6. Schlichting, H., Boundary Layer Theory, McGraw Hill, 1960, pg 21
7. Catalano, G. D., Effect of Frequency Shifting on Mean and Fluctuating Laser Velocimetry Measurements, AFFDL-TM-79-90-FXM, Wright-Patterson Air Force Base, Ohio (August 1979)
8. Catalano, G. D., private communication, Wright-Patterson AFB, Ohio
9. Prandtl, Aerodynamic Theory, Berlin (1935)
10. Catalano, G. D., Unpublished data, Wright Aeronautical Laboratories, Wright-Patterson AFB, Ohio, 1980
11. Bradshaw, P., Turbulence, Topics in Applied Physics Vol. 12, Springer-Verlag, 1978, pg 37
12. Malvern Instruments, Ltd. Operating and Installation Manual, Spring Lane Trading Estate, Malvern Link, Worcestershire WR14 1AL, England
13. Hewlett-Packard Company, Hewlett-Packard 9830A Plotter Pac, Loveland, Colorado
14. Lumley, J. G. W. and Kobaski, Y., Proceedings of the Symposium on Measurement of Turbulence in Liquids, University of Missouri at Rolla, Plenum Press, 1970

15. Morton, J. B., Experimental Measurement of Ambiguity Noise in a Laser Anemometer, Journal of Physics E, Scientific Instruments Vol. 6, January-June 1973
16. Catalano, G. D., An Experimental Investigation of a Three Dimensional Wall Jet, PhD Dissertation, University of Virginia, Charlottesville, Virginia (May 1977)

APPENDIX A

MEAN VELOCITY AND TURBULENT INTENSITY

DATA REDUCTION

Longitudinal mean velocities and turbulent intensities are computed from a typical autocorrelation function shown in Figure 38. This autocorrelation function has been corrected for skewness (Appendix B). The computational process can vary, depending upon whether a frequency shift has been applied to the phase modulator or not. Recall that frequency shifts are required in regions of high velocity or high turbulence and for determining flow direction. For the case of no frequency shifting (turbulent intensities generally less than 30%) the required expressions are as follows (Reference 12).

For the mean velocity the formula is:

$$U = \frac{S}{T_2}$$

where: S = fringe spacing in the control volume

T_2 = time to the autocorrelation function second maxima
at R_2

The fringe spacing itself is calculated according to:

$$S = \frac{\ell}{d} \frac{\lambda}{\eta}$$

where: ℓ = distance from the focusing lens to the control volume

d = separation of the laser beams at the focusing lens

λ = wavelength of the laser beam

η = refractive index (air = 1.0)

For the turbulent intensity calculations:

$$\frac{U_{RMS}}{U_{FS}} = \frac{1}{\Pi} \left[\frac{1}{2} (r-1) + \frac{1}{2N^2} \right]^{1/2} \times \frac{U_{REF}}{U_{FS}}$$

where: $r = \frac{R_2 - R_1}{R_2 - R_3}$

R_1 = autocorrelation function first minima

R_2 = autocorrelation function second maxima

R_3 = autocorrelation function second minima

$$N = \frac{r_o}{S} = \text{number of fringes in the control volume}$$

$$= \text{laser beam radius/fringe spacing}$$

In this investigation the term in the expression for turbulent intensity containing N , is neglected since its value is negligible (1.65×10^{-3}).

In the case where a frequency shift is required (high velocity or high turbulence) the expressions are as follows.

For mean velocity:

$$U = \frac{Fd \lambda}{2 \sin (2\alpha)}$$

where: F_d =Doppler frequency of the flow without a frequency shift

 λ = wavelength of the laser beam

α = half angle between the laser beams at the control volume

The doppler frequency of the flow without a frequency shift is in turn defined as:

$$F_d = F_d^* + \Delta F$$

where: F_d^* = Doppler frequency of the flow with a frequency shift

ΔF = frequency shift applied (sign depends on flow direction)

Then, the doppller frequency of the flow with the frequency shift is defined as:

$$F_d^* = \frac{2U^* \sin(2\alpha)}{\lambda}$$

where: U^* = mean velocity calculated without frequency shift

For turbulent intensity calculations:

$$\frac{U_{RMS}}{U_{FS}} = \frac{U_{RMS}^*}{U_{REF}} \left(1 + \frac{\Delta F}{F d^*} \right) \times \frac{U_{REF}}{U_{FS}}$$

where: $\frac{U_{RMS}^*}{U_{REF}}$ = turbulent intensity calculated without frequency shift

Finally, for the formula for turbulent intensities to be applied meaningfully, the autocorrelation function must be corrected for skewness (Appendix B).

APPENDIX B

SKEWED AUTOCORRELATION FUNCTION CORRECTION PROCEDURE

If the measured autocorrelation function is skewed, either due to a small number of control volume fringes or detection of background scattered light, it must first be corrected, before accurate turbulent intensity values can be calculated. Mean velocity calculations are not affected by the autocorrelation function skewness.

A typical skewed autocorrelation function is shown in Figure 37 for the flowfield location $X/2Ro=0.5$, $Y/2Ro=0.0$. To correct for skewness, a least squares fit polynomial regression routine (Reference 13) is utilized. A second degree polynomial is fitted to the first three autocorrelation function maxima and another second degree polynomial is fitted to the first three autocorrelation function minima. The resulting polynomial coefficients are respectively A_0, A_1, A_2 and B_0, B_1, B_2 and the polynomial equations of the form:

$$F_1(T) = A_0 + A_1 T + A_2 T^2$$

$$F_2(T) = B_0 + B_1 T + B_2 T^2$$

The arithmetic mean of these coefficients is taken yielding

$$C_0 = \frac{A_0 + B_0}{2}, \quad C_1 = \frac{A_1 + B_1}{2}, \quad C_2 = \frac{A_2 + B_2}{2}$$

and a new "mean parabola" of the form

$$F_3(T) = C_0 + C_1 T + C_2 T^2$$

is constructed as in Figure 37.

This curve represents the new reference datum for the skewness corrected autocorrelation function. The mean curve is then subtracted from the previous maxima and minima curve fits at points R_1 , R_2 and R_3 .

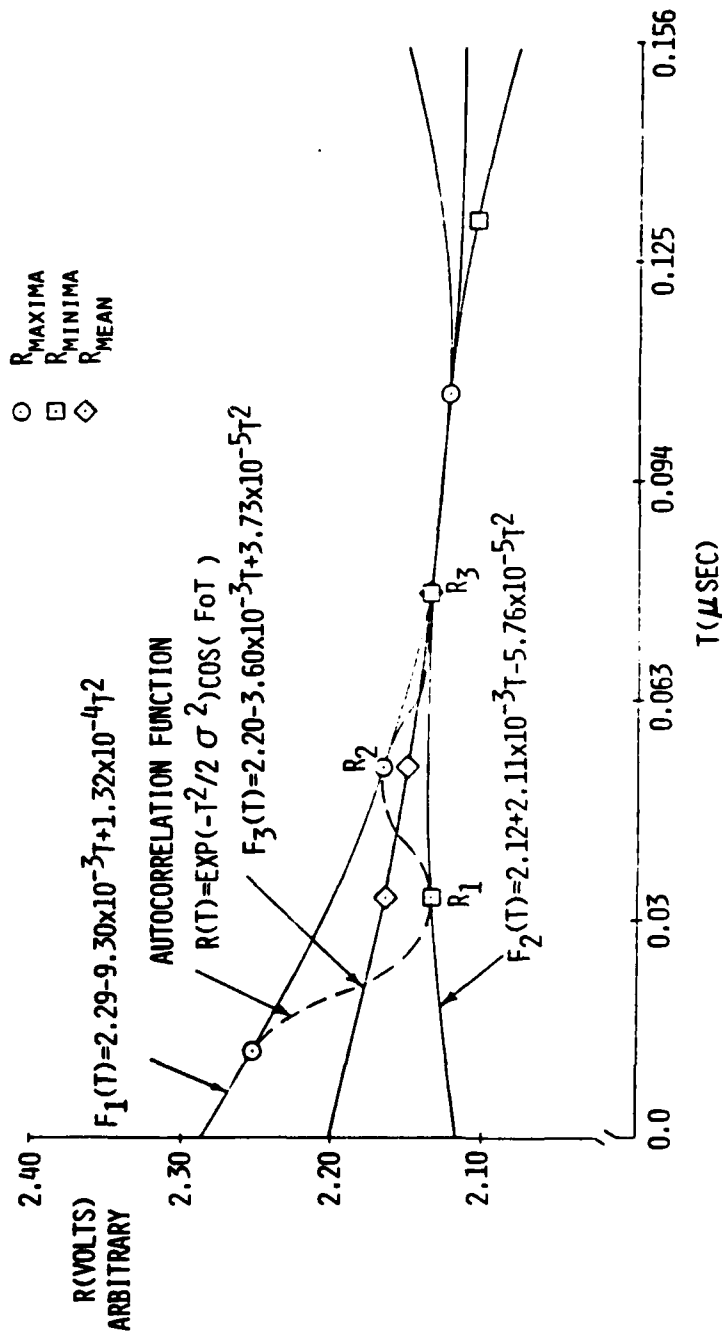


FIGURE 37. AUTOCORRELATION FUNCTION WITH SKEWNESS

The resulting differences are replotted with a subsequent shift of the mean parabola to the X axis (Figure 38). The corrected autocorrelation function is now available for turbulent intensity calculations (Appendix A).

The failure of the computational schemes presented in Appendix A, when applied to a highly skewed autocorrelation function, are a consequence of the fact that, in these cases $(R_2 - R_3) > (R_2 - R_1)$, resulting in r values less than one (undefined turbulent intensities). This technique is applicable to all autocorrelation functions above a skewness of zero.

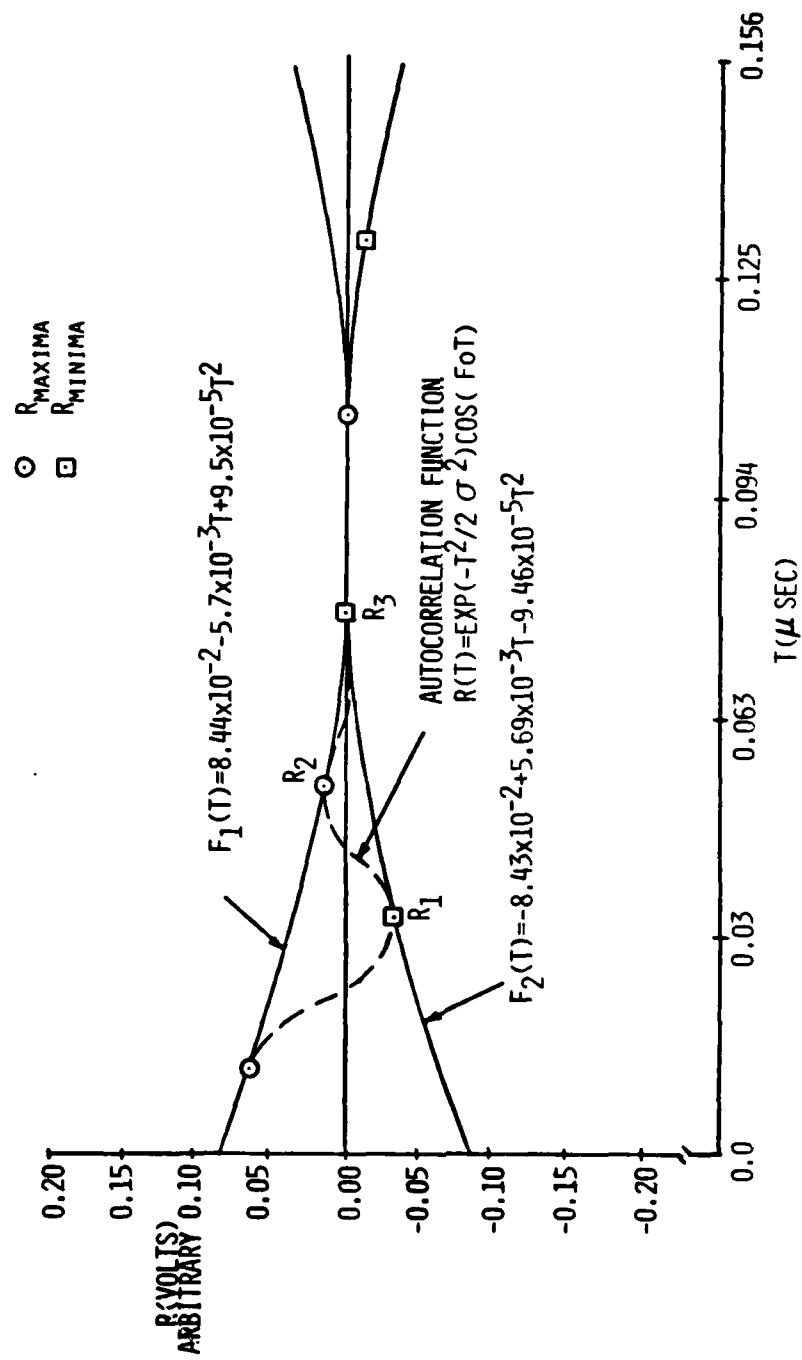


FIGURE 38. AUTOCORRELATION FUNCTION CORRECTED FOR SKEWNESS

APPENDIX C

AMBIGUITY NOISE CORRECTION

Ambiguity noise is due to the finite size of the laser measuring volume. The resultant finite transit times of marking particles as they pass through the fringes in a random manner causes an apparent turbulence to be seen.

Reference 15 states that the ambiguity noise from the autocorrelation function at $T=0.0$ should be a constant dependent on optical setup geometry.

The autocorrelation function is determined from the power spectra as derived by Lumley (Reference 14)

$$P'(F) = \frac{1}{4} [\text{EXP}\{-(F+F_0)^2 \sigma^2 / 2\} + \text{EXP}\{-(F-F_0)^2 \sigma^2 / 2\}] \quad (1)$$

by taking its Fourier transform yielding:

$$R(T) = \text{EXP}(-T^2 / 2\sigma^2) \text{COS}(F_0 T) \quad (2)$$

where: F_0 = doppler frequency

σ = a constant

The ambiguity noise is then defined as:

$$\frac{\Delta F_0}{F_0} = \frac{1}{\sigma F_0} \quad (3)$$

where: ΔF_0 = root mean square deviation from the doppler frequency

According to Reference 15 an expression for σF_0 can be determined from the formula for the doppler frequency

$$F_0 = \frac{4\pi U \sin \alpha}{\lambda} \quad (4)$$

where: U = local mean velocity

α = half angle between laser beams at the control volume

λ = laser beam wavelength

by inserting the constant σ yielding:

$$\sigma F_o = \frac{4\pi (\sigma U) \sin \alpha}{\lambda} \quad (5)$$

From the expression for the autocorrelation function, the quantity σU can be related to the distance between the $1/e^2$ points of the laser beam

$$d_* = 2\sqrt{2} (\sigma U) \quad (6)$$

which is also equal to the theoretical diameter of the laser beams at the focal point:

$$d_T = \frac{\lambda f}{r_o \Pi} \quad (7)$$

where: f = focal length of the lens

d_T = distance between $1/e$ points

r_o = laser beam radius entering lens

Equating (6) and (7) a value for σU can be determined, which is then used in expression (5) to find σF_o . The reciprocal of σF_o then represents the correction due to ambiguity noise required of the autocorrelation function.

For this investigation the value of $\Delta F_o/F_o$ was determined to be 3.9%. This value is then subtracted from the turbulent intensities calculated to arrive at a correction for ambiguity noise. The actual steps in the calculation are given below:

$$\begin{aligned} d_T &= \frac{2(6328 \times 10^{-10} \text{ m})(1 \text{ m})}{\Pi(0.0011 \text{ m})} \\ &= 3.66 \times 10^{-4} \text{ m} \end{aligned}$$

$$\sigma_U = \frac{3.66 \times 10^{-4} \text{ m}}{2\sqrt{2}}$$

$$= 1.29 \times 10^{-4} \text{ m}$$

$$\sigma_{Fo} = \frac{4\pi(1.29 \times 10^{-4} \text{ m})(0.01)}{6328 \times 10^{-10} \text{ m}}$$

$$= 25.7$$

$$\frac{1}{\sigma_{Fo}} = \frac{\Delta F_o}{F_o} = \frac{1}{25.7} = 0.0389$$

APPENDIX D

INTEGRAL TIME SCALE DETERMINATION

The integral scale is defined as the largest turbulent scale existing in a flowfield. In the photon correlation scheme, the autocorrelation function is defined in terms of the particle transit time between the fringes of the control volume. For the integral time scale determination, the time to the first zero crossing of the autocorrelation function is used (Figure 39, Reference 8). That is, the integral velocity scale is first determined using this zero crossing time as follows:

$$U_{IS} = \frac{S}{T_{C_{IS}}}$$

where: S = fringe spacing

$T_{C_{IS}}$ = time to the first autocorrelation zero crossing

This represents the velocity of the large scale disturbances in passing one fringe spacing. From this velocity and the fringe spacing, a frequency of the integral scale disturbances can be determined

$$F_{IS} = \frac{U_{IS}}{S}$$

and, proceeding one step further the integral time can be determined as:

$$T_{IS} = \frac{1}{F_{IS}}$$

Integral time scales computed by this method are of the same order of magnitude, but larger than, the Taylor time microscales computed by a similar method.

Finally, the integral time scales computed by this method should be viewed in terms of trends over the flowfield and not in terms of absolute values due to the approximate nature of this calculation.

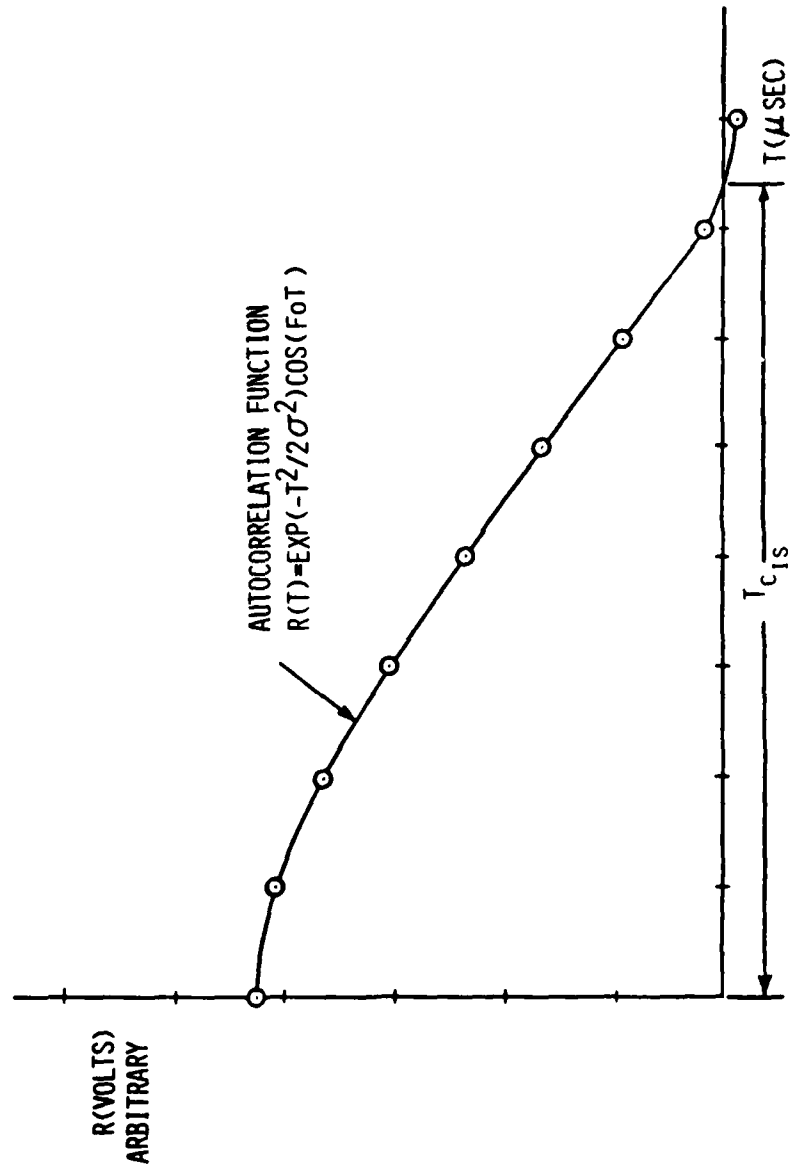


FIGURE 39. AUTOCORRELATION FUNCTION FOR INTEGRAL TIME SCALE DETERMINATION

APPENDIX E

TAYLOR TIME MICROSCALE DETERMINATION

The Taylor microscale is the characteristic turbulent scale present in a flowfield. It lies between the integral scale and the Kolmogorov scale (smallest scale present in a flowfield).

The first step in the determination of the Taylor time microscale is to fit a parabola to the autocorrelation function near $T=0.0$ (Figure 40). Ideally, this parabola should correspond closely with the first few data points of the autocorrelation function (Reference 16).

This procedure was altered for this investigation by fitting a parabola to the first two autocorrelation function points excluding the $T=0.0$ point. This, effectively eliminates any inaccuracies due to ambiguity noise present at $T=0.0$.

Due to the low number of autocorrelation function points between $T=0.0$ and $T=T_c$ a parabolic fit to the first two eligible points represents a higher percentage of the autocorrelation function curve itself than just the accepted first few data points. Since the Taylor time microscales are based upon the value of $T_{C_{MS}}$, it can be expected that the altered procedure will result in Taylor time microscales whose absolute values will be inaccurate. However, applying the procedure uniformly to all autocorrelation functions should result in observable trends.

Once the parabolic fit has been accomplished and $T_{C_{MS}}$ determined; calculation of the Taylor time microscales proceeds in a fashion similar to the integral time scale calculations. The Taylor velocity scale can be determined as:

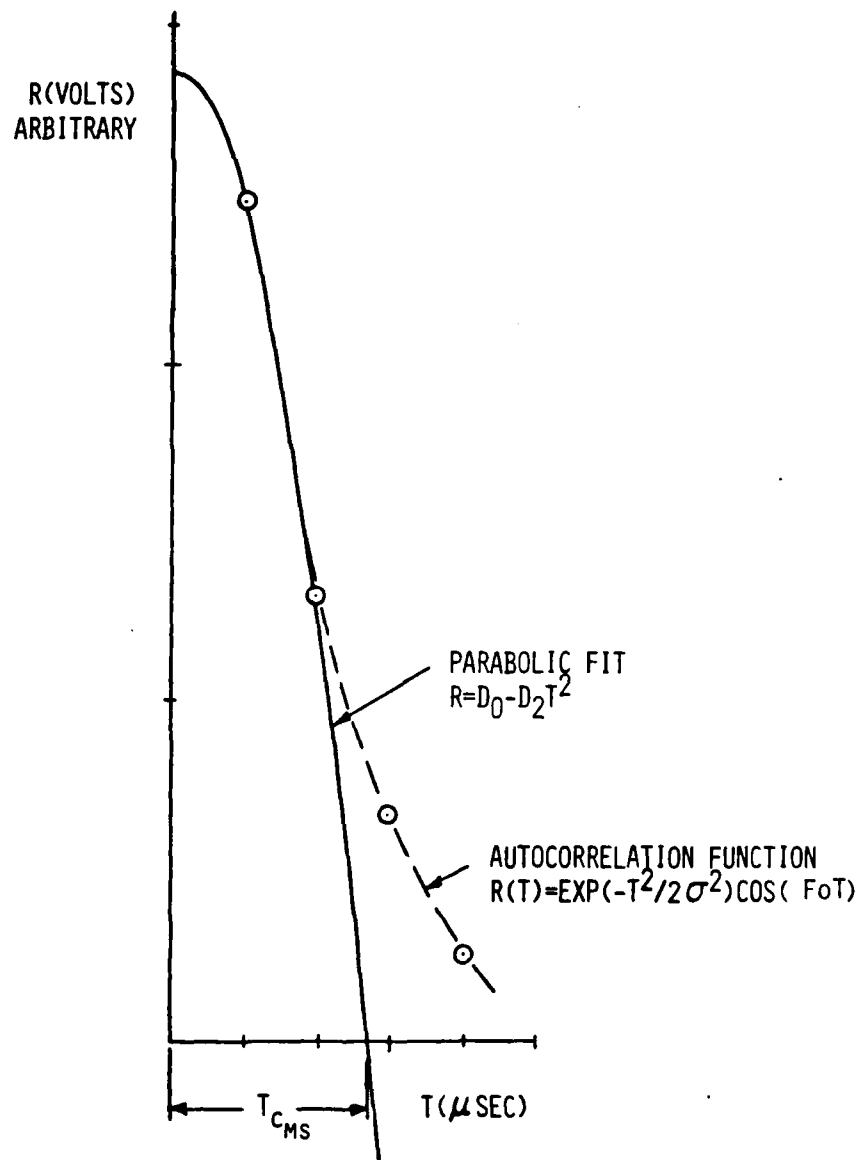


FIGURE 40. AUTOCORRELATION FUNCTION FOR TAYLOR TIME MICROSCALE DETERMINATION

$$U_{\lambda} = \frac{S}{T_{C_{MS}}}$$

where: S = fringe spacing

$T_{C_{MS}}$ = time to the intersection of the parabola with the T axis

In turn a Taylor microscale frequency is defined as

$$F_{\lambda} = \frac{U_{\lambda}}{S}$$

and the desired Taylor time microscale is the inverse of the Taylor microscale frequency:

$$T_{\lambda} = \frac{1}{F_{\lambda}}$$

As with the integral time scale calculations, absolute values of T_{λ} are apt to be subject to error. Most use of them will come in observing their trends.

AD-A091 084

AIR FORCE INST OF TECH WRIGHT-PATTERSON AFB OH SCHOO--ETC F/G 20/4
AN EXPERIMENTAL INVESTIGATION OF THE NEAR WAKE OF A CIRCULAR CY--ETC(U)
SEP 80 R E WALTERICK
AFIT/GAE/AA/805-1

UNCLASSIFIED

NL

2.1.4



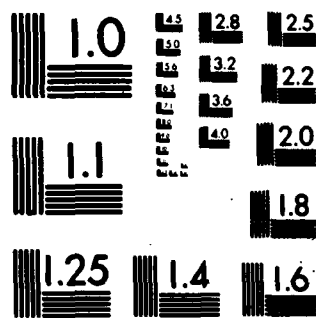
END

DATE

FILED

12.9.80

DTIC



MICROCOPY RESOLUTION TEST CHART
NATIONAL BUREAU OF STANDARDS-1963-A

APPENDIX F

PARTICLE LAG ESTIMATION

The question of whether a particle in a flowfield follows the fluid motion or not, is of primary concern to any investigation utilizing a laser velocimeter. The velocity that is actually measured by the laser velocimeter is that of the particles and not the fluid. Regions of high acceleration or deceleration, where the particle may not follow the flow direction, are most suspect in regards to this question. Hence, flow around a two dimensional circular cylinder from the leading edge stagnation point to the upper or lower midchord, represents the most critical area of concern for this investigation, since the highest levels of acceleration are achieved here.

An analysis of particle lag (Reference 16) begins with the equation of motion of a particle in a non-uniform flow under the assumptions that, the gas density is much less than the particle density and body forces are ignored in comparison to the aerodynamic drag of the particle:

$$\frac{dU_p}{dt} = \frac{3}{4} \frac{\mu R_{ep} C_D}{\rho_p D^2} (U_g - U_p) \quad (1)$$

where: μ = coefficient of viscosity (air)

$C_D = C_D(R_{ep}, M_{FS}, \text{Knudsen no.})$
= drag coefficient of the particle

ρ_p = density of particle

D = particle diameter

U_g = gas velocity

U_p = particle velocity

$$R_{ep} = \text{Reynolds number based on particle diameter}$$

$$= \frac{\rho_g (U_g - U_p) D}{\mu}$$

From Stokes Law:

$$C_D = \frac{24}{R_{ep}} \quad (2)$$

Substituting equation (2) into equation (1) yields:

$$\frac{dU_p}{dt} = \frac{3}{4} \frac{24}{R_{ep}} \frac{\mu R_{ep}}{\rho_p D^2} (U_g - U_p) \quad (3)$$

$$\text{or} \quad \frac{dU_p}{dt} = \bar{K} (U_g - U_p) \quad (4)$$

$$\text{where: } \bar{K} = \frac{18\mu}{\rho_p D^2} = \text{Stokes coefficient}$$

Particle sizes normally used for flow seeding in laser velocimeter applications, are of the order of 1 micron diameter or less. Particle sizes resulting from vaporization of kerosene are assumed to be larger and for this particle lag estimation a particle size of 5 microns diameter will be assumed.

Computing Stokes coefficient from the following parameters:

$$D = 5 \mu\text{m} = 5 \times 10^{-6} \text{ m}$$

$$\mu_{\text{air}} = 1.796 \times 10^{-5} \text{ kg/m sec}$$

$$\rho_p = 1.4 \times 10^3 \text{ kg/m}^3$$

we obtain:

$$\bar{K} = \frac{18(1.796 \times 10^{-5} \text{ kg/m sec})}{(1.4 \times 10^3 \text{ kg/m}^3)(5 \times 10^{-6} \text{ m})^2} = 9.2 \times 10^3$$

Assuming, in the worst case situation for a two dimensional cylinder,

that the flow velocity increases from 0 to 5.9 m/sec (U_{FS} for this investigation) within 0.059 m (radius of the circular cylinder), then

U_g can be assumed to vary linearly as:

$$U_g = \beta X \text{ where } \beta=100 \quad (5)$$

If the particle lag can be expressed as $\underline{U} = U_g - U_p$ then substitution of this expression into equation (4) and making the assumption that $\underline{U} \ll U_g$ results in:

$$U_g \frac{dU_g}{dx} = U_g \frac{d\underline{U}}{dx} + \bar{K} \underline{U} \quad (6)$$

Inserting equation (5) into equation (6) yields:

$$\beta^2 X = \beta X \frac{d\underline{U}}{dx} + \bar{K} \underline{U} \quad (7)$$

Integrating and assuming $\underline{U} = 0$ at $X = 0$, then:

$$\underline{U} = \frac{\beta^2}{\beta + \bar{K}} X = \frac{\beta}{\beta + \bar{K}} U_g \quad (8)$$

Substituting β and \bar{K} for this investigation into (8) gives:

$$\underline{U} = \frac{100 U_g}{100 + 9.2 \times 10^3} = 1.08 \times 10^{-2} U_g$$

The particle lag is one percent of the gas mean velocity. Since this calculation is performed for the region of highest flow acceleration, the particle lag in less accelerated regions can be assumed to be less than one percent. Therefore particle lag is considered to be negligible for this investigation.

VITA

Ronald Eugene Walterick was born on 22 March 1951 in Alexandria, Virginia. He graduated from high school in Vienna, Virginia in 1969 and attended the Georgia Institute of Technology from which he received the degree of Bachelor of Aerospace Engineering, Co-Operative Plan in August 1974. Upon graduation he was employed as an experimental aerodynamics engineer for the Air Force Flight Dynamics Laboratory until entering the School of Engineering, Air Force Institute of Technology, in September 1979.

Permanent address: 5431 Idlewood Road, Dayton, Ohio 45432

UNCLASSIFIED

SECURITY CLASSIFICATION OF THIS PAGE (When Data Entered)

REPORT DOCUMENTATION PAGE		READ INSTRUCTIONS BEFORE COMPLETING FORM	
1. REPORT NUMBER	2. GOVT ACCESSION NO.	3. RECIPIENT'S CATALOG NUMBER	
AFIT/GAE/AA/80S-1	AD-A091084		
4. TITLE (and Subtitle)		5. TYPE OF REPORT & PERIOD COVERED	
AN EXPERIMENTAL INVESTIGATION OF THE NEAR WAKE OF A CIRCULAR CYLINDER		MS THESIS	
7. AUTHOR(s)		6. PERFORMING ORG. REPORT NUMBER	
RONALD E. WALTERICK CIV USAF			
9. PERFORMING ORGANIZATION NAME AND ADDRESS		8. CONTRACT OR GRANT NUMBER(s)	
Air Force Institute of Technology (AFIT-EN) Wright-Patterson AFB, OH 45433			
11. CONTROLLING OFFICE NAME AND ADDRESS		10. PROGRAM ELEMENT, PROJECT, TASK AREA & WORK UNIT NUMBERS	
14. MONITORING AGENCY NAME & ADDRESS (if different from Controlling Office)		12. REPORT DATE	
		September 1980	
		13. NUMBER OF PAGES	
		15. SECURITY CLASS. (of this report)	
		Unclassified	
		15a. DECLASSIFICATION DOWNGRADING SCHEDULE	
16. DISTRIBUTION STATEMENT (of this Report)			
Approved for public release; distribution unlimited			
17. DISTRIBUTION STATEMENT (of the abstract entered in Block 20, if different from Report)			
18. SUPPLEMENTARY NOTES			
Approved for public release; IAW AFR 190-17 25 SEP 1980			
<p><i>Fredric C. Lynch</i> FREDRIC C. LYNCH, Major, USAF Director of Public Affairs Air Force Institute of Technology (ATC) Wright-Patterson AFB, OH 45433</p>			
19. KEY WORDS (Continue on reverse side if necessary and identify by block number)			
Laser Velocimeter Wakes Velocity Profiles Mean Velocity Turbulence Intensity			
20. ABSTRACT (Continue on reverse side if necessary and identify by block number)			
The near field region of the turbulent wake behind a rotating and nonrotating two dimensional circular cylinder is documented. U component mean velocities, turbulent intensities and velocity autocorrelation functions are measured at various downstream locations. From the autocorrelation functions, Taylor time microscales, longitudinal integral time scales and energy dissipation rates are computed. The measurements are performed for the flow over a circular cylinder at 100 RPM and 500 RPM. The free stream velocity and Reynolds number, based on cylinder diameter, are respectively 5.9 m/sec and approximately 50,000.			

DD FORM 1 JAN 73 1473

EDITION OF 1 NOV 65 IS OBSOLETE

UNCLASSIFIED

SECURITY CLASSIFICATION OF THIS PAGE (When Data Entered)

A

UNCLASSIFIED

SECURITY CLASSIFICATION OF THIS PAGE(When Data Entered)

✓ The turbulent measurements are made with a laser velocimeter using a frequency shifting phase modulator and the photon correlation processing scheme. Naturally occurring contaminant is augmented with vaporized kerosene to increase the magnitude of scattered light. Results are presented for the effects of varying ^{Omega}_{sc}, frequency shifting, particle concentrations and detector optics pinhole size on the turbulent quantities. ←

UNCLASSIFIED

SECURITY CLASSIFICATION OF THIS PAGE(When Data Entered)

B